Atmos. Chem. Phys. Discuss., 14, 6863–6949, 2014
www.atmos-chem-phys-discuss.net/14/6863/2014/
doi:10.5194/acpd-14-6863-2014

Atmospheric Chemistry and Physics Discussions

A global model simulation of present and future nitrate aerosols and their direct radiative forcing of climate

D. A. Hauglustaine[1,3], **Y. Balkanski**[1], **and M. Schulz**[2]

[1]Laboratoire des Sciences du Climat et de l'Environnement (LSCE), UMR 8212, CEA-CNRS-UVSQ, Gif-sur-Yvette, France
[2]Norwegian Meteorological Institute, Blindern, Norway
[3]Laboratoire Image Ville Environnement (LIVE), UMR 7362, CNRS-UdS, Strasbourg, France

Received: 21 January 2014 – Accepted: 17 February 2014 – Published: 14 March 2014

Correspondence to: D. A. Hauglustaine (didier.hauglustaine@lsce.ipsl.fr)

Published by Copernicus Publications on behalf of the European Geosciences Union.

Abstract

The ammonia cycle and nitrate particle formation have been introduced in the LMDz-INCA global model. Both fine nitrate particles formation in the accumulation mode and coarse nitrate forming on existing dust and sea-salt particles are considered. The model simulates distributions of nitrates and related species in agreement with previous studies and observations. The calculated present-day total nitrate direct radiative forcing since the pre-industrial is $-0.056\,\mathrm{W\,m^{-2}}$. This forcing has the same magnitude than the forcing associated with organic carbon particles and represents 18 % of the sulfate forcing. Fine particles largely dominate the nitrate forcing representing close to 90 % of this value. The model has been used to investigate the future changes in nitrates and direct radiative forcing of climate based on snapshot simulations for the four Representative Concentration Pathway (RCP) scenarios and for the 2030, 2050 and 2100 time horizons. Due to a decrease in fossil fuel emissions in the future, the concentrations of most of the species involved in the nitrate-ammonium-sulfate system drop by 2100 except for ammonia which originates from agricultural practices and for which emissions significantly increase in the future. Despite the decrease of nitrate surface levels in Europe and Northern America, the global burden of accumulation mode nitrates increases by up to a factor of 2.6 in 2100. This increase in nitrate in the future arises despite decreasing NO_x emissions due to increased availability of ammonia to form ammonium nitrate. The total aerosol direct forcing decreases from its present-day value of $-0.234\,\mathrm{W\,m^{-2}}$ to a range of -0.070 to $-0.130\,\mathrm{W\,m^{-2}}$ in 2100 based on the considered scenario. The direct forcing decreases for all aerosols except for nitrates for which the direct negative forcing increases to a range of -0.060 to $-0.115\,\mathrm{W\,m^{-2}}$ in 2100. Including nitrates in the radiative forcing calculations increases the total direct forcing of aerosols by a factor of 1.3 in 2000, by a factor of 1.7–2.6 in 2030, by 1.9–4.8 in 2050 and by 6.4–8.6 in 2100. These results show that agricultural emissions of ammonia will play a key role in the future mitigation of climate change with nitrates becoming the dominant contributor to the anthropogenic aerosol optical depth during

ACPD
14, 6863–6949, 2014

the second half of the XXIst century and significantly increasing the calculated aerosol direct forcing. This significant increase in the influence that nitrate exert on climate in the future will at the same time affect regional air quality and nitrogen deposition to the ecosystems.

1 Introduction

The formation of ammonium nitrate particles in the atmosphere is a secondary process initiated by the oxidation of NO_2 to nitric acid (HNO_3) and by its further reaction with ammonia (NH_3). HNO_3 can also be absorbed on existing particulate matter to form coarse nitrate aerosols (Li and Shao, 2009). Nitrogen oxides emissions are mostly associated with fossil fuel combustion (40 %), land use practices (15 %) and soils emissions (10 %) (Olivier et al., 1998). In contrast, global ammonia emissions into the atmosphere are dominated by agricultural practices (Bouwman et al., 1997). In western Europe and in the United States as much as 90–100 % of NH_3 emissions results from animal and crop agriculture (Sutton et al., 2000; Hertel et al., 2011). In the atmosphere, NH_3 reacts not only with HNO_3 but also with other acid gases such as H_2SO_4 to form ammonium (NH_4^+) containing particles. Atmospheric nitrate particles have an adverse impact on health. In Europe, for instance, these particles account today for about 10–20 % of the total dry aerosol mass (Putaud et al., 2004a; Schaap et al., 2004). These particles also contribute to the deposition of nitrogen to the surface with a cascade of advert effects on terrestrial and aquatic ecosystems and possible consequences for the global carbon cycle (Gruber and Galloway, 2008). Moreover, nitrate particles have the potential to directly affect the Earth's radiation budget by reflecting solar radiation and climate through their effect on cloud formation and precipitation (Forster et al., 2007).

Several global models have been used to simulate the nitrate-ammonium-sulfate aerosol system and their impact on the present-day climate (e.g., van Dorland et al., 1997; Adams et al., 2001; Jacobson, 2001; Martin et al., 2004; Liao and Seinfeld, 2005; Myhre et al., 2006; Bauer et al., 2007; Bellouin et al., 2011; Xu and Pen-

ACPD
14, 6863–6949, 2014

ner, 2012). These earlier studies have reported forcings ranging from $-0.02\,W\,m^{-2}$ to $-0.19\,W\,m^{-2}$. The uncertainty on the nitrate particle radiative forcing of climate remains high. Recently, Myhre et al. (2013) compiled the nitrate forcings calculated in the framework of AeroCom phase II by 8 global models and derived a present-day direct radiative forcing for the most recent model versions ranging from $-0.03\,W\,m^{-2}$ to $-0.17\,W\,m^{-2}$ and a mean of $-0.10\pm0.04\,W\,m^{-2}$. For the ACCMIP historical simulations, Shindell et al. (2013) derived a direct forcing for nitrates ranging from $-0.03\,W\,m^{-2}$ to $-0.41\,W\,m^{-2}$, with a mean of $-0.19\pm0.18\,W\,m^{-2}$. Fewer studies have assessed the future radiative forcing of nitrate particles. Adams et al. (2001), Liao and Seinfeld (2005), and Liao et al. (2009) investigated the future evolution of nitrates under the emission scenario SRES A2 and derived a direct anthropogenic radiative forcing reaching −0.95 to $-1.28\,W\,m^{-2}$ in 2100. Bauer et al. (2007) also investigated the evolution of nitrates in 2030 following the SRES A1B emission scenario. All these studies pointed out the steady increase of nitrate aerosols since industrialization and associated direct radiative forcing of climate. They also suggest that the decreased radiative forcing from sulfates particles in the future associated with reduced emissions of SO_2 could be partially offset by the increased nitrate forcing since the formation of ammonium nitrates is favored at lower sulfate loadings. More recently Bellouin et al. (2011) included nitrate aerosols in their future CMIP5 simulations driven by the RCP scenarios and indicated that nitrates could become an important aerosol species in the future making the aerosol radiative forcing 2–4 times stronger by 2100.

In this paper, the atmospheric ammonia cycle and nitrate particle formation are introduced in the LMDz-INCA global three-dimensional climate-chemistry model. Numerous detailed models have been developed in order to treat the partitioning of nitrate and ammonium between the gas phase and the aerosol phase assuming thermodynamical equilibrium between phases (e.g., Pilinis and Seinfeld, 1987; Zhang et al., 2000; Metzger et al., 2002a, 2006) or treating the dynamical mass transfer between each aerosol size bin explicitly (e.g., Pilinis et al., 2000; Jacobson et al., 1999; Jacobson, 1999; Sun and Wexler, 1998; Lauer et al., 2005). In order to apply these computa-

ACPD
14, 6863–6949, 2014

tionally expensive models at the global scale, several authors have chosen to apply parameterizations for the relationships between activity coefficients and the relative humidity (Metzger et al., 2002a, b; Myhre et al., 2006; Bauer et al., 2007; Pringle et al., 2010) or to use an hybrid dynamic method (Feng and Penner, 2007; Xu and Penner, 2012). In this study, since the LMDz-INCA general circulation model is designed for long term simulations, we also use a simplified approach, and the phase equilibrium of the ammonium-sulfate-nitrate aerosol system is introduced for fine particles based on the simple thermodynamical formulation used initially in regional acid deposition chemical transport models (Hov et al., 1988; Ackermann et al., 1995), in global chemical transport models (Tie et al., 2005), and more recently in an Earth system model (Bellouin et al., 2011). In addition to this formation of fine nitrate particles in the accumulation mode, the role of nitric acid uptake on mineral dust and sea-salt particles to form coated coarse nitrate particles can also play an important role in the total nitrate and nitric acid budget in the atmosphere and hence on the radiative forcing (e.g., Liao and Seinfeld, 2005; Myhre et al., 2006; Bauer et al., 2007; Feng and Penner, 2007; Xu and Penner, 2012). The formation of coarse nitrate particles on dust and on sea-salt particles is also introduced in LMDz-INCA adopting a first–order removal. This method is computationally efficient and has often been used in global models (e.g., Dentener and Crutzen, 1993; Bauer et al., 2004, 2007; Evans et al., 2005; Fairlie et al., 2010) despite the fact that limitations for this formulation exist (Feng and Penner, 2007). An evaluation of the simulated aerosol distributions calculated with the LMDz-INCA model, of the optical depth and surface nitrate and sulfate depositions are performed. Based on the recent RCP CMIP5 emission scenarios we then use the model to calculate the present-day and future anthropogenic direct radiative forcing of fine and coarse nitrate particules and to assess the relative contribution of nitrates to the aerosol optical depth and radiative forcing.

The three-dimensional global model used in this study and the extension of the chemical and aerosol scheme to include ammonia and nitrate particles are described in Sect. 2. Section 3 presents the present-day global distributions of aerosols, the eval-

ACPD
14, 6863–6949, 2014

uation of the model results and the direct radiative forcing of aerosols. The results of the future simulations in terms of atmospheric composition, surface deposition and direct radiative forcing of climate are presented in Sect. 4. Finally, Sect. 5 gives the summary and conclusions.

2 Model description

2.1 The LMDz-INCA model

We use the LMDz-INCA global chemistry-aerosol-climate model coupling on-line the LMDz (**L**aboratoire de **M**étéorologie **D**ynamique, version 4) General Circulation Model (Hourdin et al., 2006) and the INCA (**IN**teraction with **C**hemistry and **A**erosols, version 3) model (Hauglustaine et al., 2004). The interaction between the atmosphere and the land surface is ensured through the coupling of LMDz with the ORCHIDEE (**OR**ganizing **C**arbon and **H**ydrology **I**n **D**ynamic **E**cosyste**m**s, version 9) dynamical vegetation model (Krinner et al., 2005). In the present configuration, the model includes 19 hybrid vertical levels extending up to 4 hPa, and a horizontal resolution of 1.9° in latitude and 3.75° in longitude. The primitive equations in the GCM are solved with a 3 min time-step, large-scale transport of tracers is carried out every 15 min, and physical and chemical processes are calculated at a 30 min time interval. For a more detailed description and an extended evaluation of the GCM we refer to Hourdin et al. (2006). The large-scale advection of tracers is calculated based on a monotonic finite-volume second-order scheme (Van Leer, 1977; Hourdin and Armengaud, 1999). Deep convection is parameterized according to the scheme of Emanuel (1991). The turbulent mixing in the planetary boundary layer is based on a local second-order closure formalism.

INCA includes a state-of-the-art CH_4-NO_x-CO-NMHC-O_3 tropospheric photochemistry (Hauglustaine et al., 2004; Folberth et al., 2006). The tropospheric photochemistry and aerosols scheme used in this model version is described through a total of 123 tracers including 22 tracers to represent aerosols. The model includes 234 homo-

ACPD
14, 6863–6949, 2014

geneous chemical reactions, 43 photolytic reactions and 30 heterogeneous reactions. The gas-phase version of the model has been extensively compared to observations in the lower-troposphere (e.g., Hauglustaine et al., 2004; Folberth et al., 2006; Fiore et al., 2009; Reidmiller et al., 2009), and in the upper-troposphere (e.g., Brunner et al., 2003; Dufour et al., 2007). For aerosols, the INCA model simulates the distribution of anthropogenic aerosols such as sulfates, black carbon, particulate organic matter, as well as natural aerosols such as sea-salt and dust. The aerosol model keeps track of both the number and the mass of aerosols using a modal approach to treat the size distribution, which is described by a superposition of 5 log-normal modes (Schulz et al., 1998; Schulz, 2007), each with fixed spread. To treat the optically relevant aerosol size diversity, particle modes exist for three ranges: sub-micronic (diameter < 1 µm) corresponding to the accumulation mode, micronic (diameter between 1 and 10 µm) corresponding to coarse particles, and super-micronic or super coarse particles (diameter > 10 µm). This treatment in modes is computationally much more efficient compared to a bin-scheme (Schulz et al., 1998). Furthermore, to account for the diversity in chemical composition, hygroscopicity, and mixing state, we distinguish between soluble and insoluble modes. In both sub-micron and micron size, soluble and insoluble aerosols are treated separately. Sea-salt, SO_4 and methane sulfonic acid (MSA) are treated as soluble components of the aerosol, dust is treated as insoluble, whereas black carbon (BC) and particulate organic matter (POM) appear both in the soluble and insoluble fractions. The ageing of primary insoluble carbonaceous particles transfers insoluble aerosol number and mass to soluble with a half-life of 1.1 days (Cooke and Wilson, 1996; Chung et al., 2002).

The uptake and loss of water from aerosol particles is generally fast and depends on the chemical composition, size and surface properties of the aerosol particle. Aerosol water is responsible for about 50 % of the global aerosol column load. This water uptake modifies the aerosol optical properties. The optical depth, τ, can be expressed as a function of the effective radius of the aerosol:

$$\tau = 3QM/4\rho r_e \quad (1)$$

ACPD
14, 6863–6949, 2014

where Q is the extinction coefficient (dimensionless) computed using Mie theory, M, is the aerosol burden per unit area ($kg\,m^{-2}$), ρ is the particle density ($kg\,m^{-3}$), and r_e, the effective radius (m). As relative humidity increases, this equation has to be modified to account for the presence of water. The density is then recomputed as the mass-weighted sum of the dry density of the aerosol and the density of water. The refractive index, hence the extinction, is also changed to account for water. We use a formulation first implemented by Chin et al. (2002) to rewrite (1) as a function of the aerosol dry burden M_d ($kg\,m^{-2}$):

$$\tau = \beta M_d \tag{2}$$

where β, the specific extinction ($m^2\,kg^{-1}$), is computed as follows:

$$\beta = 3QM/4\rho r_e M_d \tag{3}$$

The optical properties and hygroscopic growth of sea-salt were taken from Irshad et al. (2005). For sulfates, we followed the relationships published for ammonium sulfate by Martin et al. (2003). In the case of black carbon and organics carbon we took the same dependence of hygroscopic growth on relative humidity as Chin et al. (2002). The aerosol scheme is thoroughly explained in Schulz (2007) and Balkanski (2011). Characteristic global aerosol properties of the INCA model have been described and compared in all AeroCom publications, as for instant recently in Myhre et al. (2013) and Koffi et al. (2012). We also refer to Szopa et al. (2012) for a simulation of the global aerosol components (excluding nitrates) and tropospheric ozone distributions and their associated radiative forcings between 1850 and 2100 following a recent historical emission dataset (Lamarque et al., 2010) and under the representative concentration pathways (RCP) (Lamarque et al., 2011) for the future with the same version of the model.

ACPD
14, 6863–6949, 2014

2.2 Ammonia and nitrate particles

The LMDz-INCA chemical scheme has been extended in order to include the ammonia cycle and the nitrate particle formation. The various NH_3 emissions have been introduced in the model as described in the next section. Ammonia undergoes several gas phase reactions which have been introduced in the model chemical mechanism but with minor contribution to the overall NH_3 cycle and impact on gas phase chemistry:

$$NH_3 + OH \rightarrow NH_2 + H_2O \quad \text{(R1)}$$
$$NH_3 + O^1D \rightarrow NH_2 + OH \quad \text{(R2)}$$
$$NH_2 + NO_2 \rightarrow N_2O + H_2O \quad \text{(R3)}$$
$$NH_2 + HO_2 \rightarrow NH_3 + O_2 \quad \text{(R4)}$$
$$NH_2 + NO \rightarrow N_2 + H_2O \quad \text{(R5)}$$
$$NH_2 + O_3 \rightarrow NH_2O + O_2 \quad \text{(R6)}$$
$$NH_2 + O_2 \rightarrow NO + H_2O \quad \text{(R7)}$$
$$NH_2O + O_3 \rightarrow NH_2 + 2O_2 \quad \text{(R8)}$$
$$NH_2O + NO \rightarrow NH_2 + NO_2 \quad \text{(R9)}$$

The rate constants for these reactions are taken from Sander et al. (2011).

The most abundant acids in the troposphere are sulfuric acid (H_2SO_4) and nitric acid (HNO_3). Ammonia acts as the main neutralizing agent for these two species. Therefore, formulating the respective aerosol particle formation scheme as a purely sulfate-nitrate-ammonia system seems to be a reasonable assumption for a global chemistry-aerosol-climate model. However, we also remove nitric acid through reaction with sea salt and dust, as described below. As a first step, ammonium sulfate is formed instantaneously and irreversibly from NH_3 and H_2SO_4, only limited by the availability of the less abundant of the two species. The concentration of NH_3 and SO_4 are depleted upon

ACPD
14, 6863–6949, 2014

formation of ammonium sulfate which takes priority over ammonium nitrate formation:

$$NH_3 + H_2SO_4 \rightarrow (NH_4)HSO_4 \quad \text{(R10a)}$$

$$3NH_3 + 2H_2SO_4 \rightarrow (NH_4)_3H(SO_4)_2 \quad \text{(R10b)}$$

$$2NH_3 + H_2SO_4 \rightarrow (NH_4)_2SO_4 \quad \text{(R10c)}$$

As in Metzger et al. (2002), three domains are considered to characterize the neutralization state of the ammonium sulfate ion formed, depending on the relative ammonia and sulfate concentrations. The total nitrate (T_N), total ammonia (T_A), and total sulfate (T_S) concentrations are defined as:

$$T_N = [HNO_3] + [NO_3^-] \quad (4)$$

$$T_A = [NH_3] + [NH_4^+] \quad (5)$$

$$T_S = [SO_4{}^{2-}] \quad (6)$$

If $T_A > 2T_S$, ammonia rich condition (sulfate state $\Gamma = 2.0$), the reaction pathway is provided by the chemical Reaction (R10c); if $T_A < 2T_S$, sulfate rich condition (sulfate state $\Gamma = 1.5$), Reaction (R10b) is considered; and if $T_A < T_S$, sulfate very rich condition (sulfate state $\Gamma = 1.0$), the reaction occurs through Reaction (R10a).

In a second step, if all free ammonia is consumed by the sulfate forming reaction, no ammonium nitrate is formed. If free ammonia persists, it is used for the neutralization of nitric acid to ammonium nitrate aerosol following the equilibrium reaction:

$$HNO_3 + NH_3 \leftrightarrow NH_4NO_3 \quad \text{(R11)}$$

The equilibrium constant (K_p) of Reaction (R11) strongly depends on relative humidity and temperature. The parameterization used for this dependence is based on Mozurkewich (1993). First, the deliquescence relative humidity (DRH, %) is calculated based on Seinfeld and Pandis (1998):

$$DRH = \exp(723.7/T + 1.6954) \quad (7)$$

ACPD
14, 6863–6949, 2014

where T is the air temperature (K). For relative humidities lower than DRH, $K_p = K_{pd}$ and is calculated with:

$$K_{pd} = \exp[118.87 - 24\,084/T - 6.025\ln(T)] \quad (8)$$

For relative humidities higher than DRH, $K_p = K_{ph}$ and depends on both temperature and relative humidity (RH) and is calculated based on:

$$K_{ph} = K_{pd}(p_1 - p_2 RH_1 + p_3 RH_1^2) RH_1^{1.75} \quad (9)$$

With RH_1 defined as $(1 - RH/100)$ and p_1, p_2, and p_3 provided by:

$$p_1 = \exp[-135.94 + 8763/T + 19.12\ln(T)] \quad (10)$$

$$p_2 = \exp[-122.65 + 9969/T + 16.22\ln(T)] \quad (11)$$

$$p_3 = \exp[-182.61 + 13875/T + 24.46\ln(T)] \quad (12)$$

The equilibrium concentration of ammonium nitrate is calculated based on Seinfeld and Pandis (1998). The free ammonia in the system is defined as the total ammonia minus the ammonia required to neutralize the available sulfate:

$$T_A^* = T_A - \Gamma T_S \quad (13)$$

If $T_N T_A^* > K_p$, the ammonium nitrate concentration is calculated according to:

$$[NH_4NO_3] = \frac{1}{2}\left[T_A^* + T_N - \sqrt{\left(T_A^* + T_N\right)^2 - 4\left(T_N T_A^* - K_p\right)}\right] \quad (14)$$

Elsewhere, ammonium nitrate dissociates and $[NH_4NO_3] = 0$. The concentration of NH_3 and HNO_3 are depleted or replenished to account for ammonium nitrate formation or dissociation, respectively. The chemical formation of ammonium sulfate particles

ACPD
14, 6863–6949, 2014

according to Reaction (R10) and of ammonium nitrate particles according to Reaction (R11) goes into the accumulation mode. The formation of nitrates through Reaction (R11) is also associated with a corresponding increase in the number of particles in the accumulation mode reflecting the formation of new ammonium nitrate particles.

Gaseous HNO_3 can condense on both accumulation mode and coarse particles. As in Myhre et al. (2006), first photochemistry and accumulation mode aerosol formation are solved because the smaller particles reach equilibrium faster than the larger ones. After the small particles are in equilibrium, the concentration of gaseous HNO_3 is updated for the condensation on coarse particles. We account for the heterogeneous reaction of HNO_3 with dust and sea-salt particles:

$$HNO_3 + NaCl \rightarrow NaNO_3 + HCl \quad \text{(R12)}$$

$$2HNO_3 + CaCO_3 \rightarrow Ca(NO_3)_2 + H_2CO_3 \quad \text{(R13)}$$

We use a standard first-order reactive uptake parameterisation to represent the uptake of HNO_3 on pre-existing dust and sea-salt particles in the model and formation of coarse nitrate particles (Dentener and Crutzen, 1993; Bauer et al., 2004; Fairlie et al., 2010). The rate constants k_{12} and k_{13} of Reactions (R12) and (R13), which describe the loss of HNO_3 from the gas phase, are calculated from (Schwartz, 1986):

$$k_{12,13} = \int_{r_i}^{r_f} 4\pi r^2 N(r) \left(\frac{r}{D_g} + \frac{4}{\upsilon\gamma} \right)^{-1} \mathrm{d}r \quad (15)$$

where N is the number density of dust or sea-salt particles of radius $[r, r + \mathrm{d}r]$, D_g is the calculated, pressure and temperature dependent, molecular diffusion coefficient ($\mathrm{cm^2\,s^{-1}}$), υ the calculated, temperature dependent, mean molecular speed ($\mathrm{cm\,s^{-1}}$), and γ the reactive uptake coefficient. Equation (15) is integrated from $r_i = 0.01$ to $r_f = 30\,\mu\mathrm{m}$. For the reaction on dust particles, we use the RH dependent uptake coefficient proposed by Fairlie et al. (2010). Based on this RH-dependence, γ increases from 1×10^{-5} for RH lower than 10 % up to 1.05×10^{-3} for RH larger than 80 %. As in Fairlie

ACPD
14, 6863–6949, 2014

et al. (2010), we introduce a Ca^{2+} limitation for the uptake of HNO_3 on dust through Reaction (R13). Based on dust source maps (Claquin et al., 1999), it is assumed than Ca^{2+} constitutes 5 % of the dust mass. Dust alkalinity is then consumed by the uptake of HNO_3. Once the alkalinity is titrated by the formation of nitrates, the uptake of HNO_3 through Reaction (R13) ceases. For sea-salt particles, the same dependence is used for the γ increase with RH. The values are scaled to the accommodation coefficients compiled by Sander et al. (2011) and γ increases from 1×10^{-3} for RH lower than 10 % up to 1×10^{-1} for RH larger than 80 %. No alkalinity limitation is considered for sea-salt particles.

These new gaseous species and particles introduced in the model to represent the ammonia cycle, the formation of ammonium sulfate, ammonium nitrate and coarse nitrates on dust and sea-salt are subject to the same transport and mixing processes as the other tracers in the model. The dry and wet deposition of NH_3 is introduced as described by Hauglustaine et al. (2004) with an Henry's law coefficient taken from Sander et al. (2011). Ammonium nitrate and ammonium sulfate are subject to the same dry and wet deposition processes as sulfate particles already in the model and coarse nitrates on dust and sea-salt are deposited as the corresponding dust and sea-salt components, respectively.

The hygroscopic growth of ammonium nitrate has been characterized in the laboratory by measuring droplet growth for different conditions of relative humidity by Tang (1996). The optical properties of nitrate particles in the accumulation and coarse modes where obtained through Mie calculation using the refractive indices for two overlapping spectral intervals. Gosse et al. (1997) measured the refractive index of ammonium nitrate from 0.7 to 2.6 µm, whereas Jarzembski et al. (2003) covered the far visible to the infrared wavelengths from 2.0 to 20 µm. Values of specific extinction, asymmetry parameter and single scattering albedo were tabulated for eleven values of relative humidities: from 0 to 90 % with 10 % increments and finally for the 95 % value. For a given relative humidity, we interpolate between the two closest values, if relative humidity

ACPD
14, 6863–6949, 2014

exceeds 95 % then we take for optical parameters the values deduced from the Mie theory at 95 % relative humidity.

2.3 Model set-up

For the simulation of "present" (2000) and "pre-industrial" (1850) conditions, the anthropogenic emissions compiled by Lamarque et al. (2010), are added to the natural fluxes used in the INCA model. All natural emissions are kept at their present-day levels. For organic aerosols, the secondary organic matter formed from biogenic emissions is equal to that provided by the AEROCOM emission dataset (Dentener et al., 2006a). The ORCHIDEE vegetation model has been used to calculate off-line the biogenic surface fluxes of isoprene, terpenes, acetone and methanol as well as NO soil emissions as described by Lathière et al. (2006). NH_3 emissions from natural soils and ocean are taken from Bouwman et al. (1997). Natural emissions of dust and sea salt are computed using the 10 m wind components from the the European Center for Medium-Range Weather Forecasts (ECMWF) reanalysis for 2006 and, consequently, have seasonal cycles but no inter-annual variability. For the future simulations (2030, 2050, 2100), the four Representative Concentration Pathways (RCP) anthropogenic and biomass burning emissions provided by Lamarque et al. (2011) are used. Methodological elements used to build these projections can be found in Lamarque et al. (2011). Natural emissions for both gaseous species and particles are kept to their present-day level as described above. Table 1 gives the list of simulations performed and the corresponding total and global emissions of key species discussed in this paper. In all RCP scenarios, fossil fuel driven emissions, NO_x, SO_2, BC and OC, decrease in 2100 compared to 2000 emissions. It is however interesting to note that NH_3 emissions, driven by agriculture, increase in all scenarios from 50 Tg N in 2000 to 54–79 Tg N in 2100 depending on to the considered scenario. As will be discussed in the next sections, this feature will have major implications in terms of nitrate future radiative forcing of climate.

ACPD
14, 6863–6949, 2014

In this study, meteorological data from the ECMWF reanalysis have been used. The relaxation of the GCM winds towards ECMWF meteorology is performed by applying at each time step a correction term to the GCM u and v wind components with a relaxation time of 2.5 h (Hourdin and Issartel, 2000; Hauglustaine et al., 2004). The ECMWF fields are provided every 6 h and interpolated onto the LMDz grid. We focus this work on the distribution of nitrate particles, its evolution under future anthropogenic emissions, and its direct radiative forcing of climate. In order to isolate the impact of anthropogenic emission scenarios, all snapshot simulations are performed under present-day climate conditions and run for a period of two years. Therefore ECMWF meteorological data for 2005–2006 are used. Results for 2006 conditions are presented. The impact of climate change on particles and chemistry is therefore not included in the results. The role played by climate change and the impact of nitrate on the indirect aerosol radiative forcing of climate will be investigated in a forthcoming study.

3 Present-day distributions

3.1 Simulated aerosol distributions

In this section we present the distributions of gaseous species and aerosols involved in the formation of nitrate particles. Figure 1 shows the present-day annual mean surface concentration of sulfates (SO_4^{2-}), ammonium (NH_4^+) and total (fine + coarse) nitrates (NO_3^-) aerosols. Maximum sulfate concentrations are calculated over regions of high SO_2 emissions with marked maxima reaching 4–5 $\mu g\,m^{-3}$ over the Eastern United States, Southern and Eastern Europe and China. The concentration of ammonium (associated both with ammonium sulfate and ammonium nitrate) is localized over continental regions and reaches maxima of 1–2 $\mu g\,m^{-3}$ over the central and eastern United States, 2–3 $\mu g\,m^{-3}$ in northern Europe and 4–5 $\mu g\,m^{-3}$ in northern China. These regions combine both high concentrations of sulfates, nitric acid but also high agricultural emissions of NH_3. The distribution of surface nitrates (fine mode + coarse mode)

ACPD
14, 6863–6949, 2014

shows very strong concentrations in regions of high ammonia and nitric acid concentrations (see below). This is in particular the case over northern Europe and China with concentrations reaching 4–5 $\mu g\,m^{-3}$. The surface distributions of these three aerosol components are in general agreement with the recent global model results presented by Pringle et al. (2010) and Xu and Penner (2012) and with the nitrate distributions calculated by Myhre et al. (2006) and Bauer et al. (2007).

Figure 2 decomposes the total surface nitrate concentration shown in Fig. 1 into its three components: accumulation mode, coarse mode on dust particles and coarse mode on sea-salt particles. The conditions for fine mode nitrate particle formation (expressed by Eq. 14) are met over the continents and maximum concentrations are calculated, as already seen in Fig. 1, over regions of high agricultural emissions of NH_3 or high HNO_3 concentrations. Coarse nitrate on dust follow the distribution of dust particles in the model (Bauer et al., 2004). High concentrations reaching more than 0.5 $\mu g\,m^{-3}$, and locally up to 1–3 $\mu g\,m^{-3}$, are calculated over the Sahara desert and the Saudi Arabian peninsula and extend to the Mediterranean sea and southern Europe; over the western United States and over China. In contrast, coarse nitrate on sea-salt reaches concentrations of 0.5–1 $\mu g\,m^{-3}$ in coastal areas where high concentrations of sea-salt and nitric acid are met. These two coarse nitrate components add up for a total of about 0.1–0.2 $\mu g\,m^{-3}$ over the ocean. Over the continents, anthropogenic nitrates significantly dominate over source regions. However, in coastal regions or in southern Europe all components mix and coarse nitrates can contribute to 30–40 % to the total concentration in these specific areas. The calculated distribution of coarse nitrates on dust and sea-salt is in fairly good agreement with the results presented by Myhre et al. (2006), Bauer et al. (2007), and by Xu and Penner (2012).

In order to evaluate the model results, Fig. 3 compares the simulated and the measured surface concentrations of SO_4^{2-}, NH_4^+, and NO_3^- from the EBAS database at NILU. EBAS holds data from EMEP (emep.int), from the US National Atmospheric Deposition Program/National Trend Network (NADP/NTN; http://nadp.sws.uiuc.edu/NTN), from the US Interagency Monitoring of Protected Visual Environments (IMPROVE;

ACPD
14, 6863–6949, 2014

http://vista.cira.colostate.edu/IMPROVE), from the Clean Air Status and Trends Network (CASTNET; http://java.epa.gov/castnet) and the EANET, Data on the Acid Deposition in the East Asian Region (http://www.eanet.cc/). These comparisons have been prepared using the AEROCOM evaluation tools (Schulz et al., 2006). The aerosols measurements are mostly from the CASTNET/IMPROVE network over Northern America, from the EMEP network in Europe. This evaluation is performed for the year 2006 based on matching daily mean data, averaged to monthly means. On Fig. 3 we illustrate the correlation plots prepared for Europe and North America. Similar plots are also available for the world and other regions and for each month via the AeroCom web interface. For SO_4^{2-}, the Normalized Mean Bias (difference between the arithmetic mean of the model minus the arithmetic mean of the measurements relative to the mean measurements) is +20 % for Europe (with a correlation coefficient R between the two datasets of 0.58) and +21 % (R = 0.68) for Northern America. Worldwide the NMB is +20 % (R = 0.66). For ammonium concentrations, the evaluation shows that NH_4^+ is overestimated worldwide with a NMB of +47 % (R = 0.52). Over Europe, the NMB is +62 % (R = 0.43) and, in contrast, NH_4^+ is slightly underestimated over Northern America with a NMB of −16 % (R = 0.77). For nitrate concentrations, a worldwide overestimate is obtained with a NMB of +68 % (R = 0.59). The comparison with the measurements are more contrasted over the two regions, with smaller bias but smaller correlation over Europe (NMB = +64 %, R = 0.43) than over Northern America (NMB = +115 %, R = 0.54). For NO_3^-, the bias is mainly driven by an overestimate of observed concentrations in summer (NMB = +143 % worldwide) compared to winter (NMB = +22 %). These comparisons are fairly good considering the difficulty to represent station measurements with a large scale atmospheric model. The comparison made for a specific year (2006) using an emission inventory representative of the year 2000 as in our case is a source of bias, which we estimate to be of the order of 10–30 % for European and American sites (Schulz et al., 2013). These results are generally in line with the comparisons obtained with more detailed aerosol models (Adams et al., 1999; Park et al., 2004; Pringle et al., 2010; Xu et al., 2012; Zhang et al., 2012; Heald

ACPD
14, 6863–6949, 2014

et al., 2012) or with a model of the same complexity (Bellouin et al., 2011). In particular, these studies showed the difficulty to represent nitrates particles which is currently overestimated by a factor of two at the surface by the global models.

Figure 4 shows the column burden of SO_4^{2-}, NH_4^+, and total NO_3^-. The sulfates column reaches more than 3 mg m^{-2} over the continents in the Northern Hemisphere. In the Eastern US, Northern and Central Europe, the column reaches more than 5 mg m^{-2}. The maximum column of more than 10 mg m^{-2} is reached over China. These values are slightly higher than the column of 1–2 mg m^{-2} calculated over the continents by Pringle et al. (2010) with a more complex aerosol microphysics and partitioning model. The global mean column burden for SO_4^{2-} is 2.5 mg m^{-2}, on the upper range of the recent model intercomparison by Myhre et al. (2013), who reported a mean burden of 1.9 ± 0.5 mg m^{-2}. The evaluation of the aerosol optical depth will be important in order to evaluate those results (see below). The column burden of NH_4^+ reaches 1–3 mg m^{-2} over source regions in the Northern Hemisphere. Maximum values reaching 5–10 mg m^{-2} are calculated over Northern China. This distribution is very close to the burden calculated by Pringle et al. (2010) but exhibits somewhat lower maximum values. The global mean burden for NH_4^+ is 0.54 mg m^{-2}. The total (coarse + fine) nitrate aerosol column shows strong maximum of 5–10 mg m^{-2} over Northern and Southern Europe, over India and China and over Africa. A secondary maximum of 3–4 mg m^{-2} is also calculated over the central US. This distribution is in agreement with the burden illustrated by Myhre et al. (2006) and Pringle et al. (2010). The global mean total nitrate burden is 1.56 mg m^{-2}. Figure 5 shows the three components of this total nitrate column and shows the fine mode, coarse mode on dust and coarse mode on sea-salt separately. This figure clearly shows that fine nitrate particles associated with anthropogenic emissions contribute to a large extent to the maximum calculated in the central US, in Northern Europe and over the Po Valley, in Northern India and in China. Over Africa, Saudi Arabia, Central Europe and in Northern China, nitrates on dust contribute for more than 4–10 mg m^{-2} to the nitrate column. Over the Mediterranean and in Southern Europe, the contribution of coarse nitrates on dust represents about 50 % of the calcu-

ACPD
14, 6863–6949, 2014

lated total nitrate column, a proportion in agreement with the measurements by Putaud et al. (2004b). These results are in line with the fine and coarse particles plumes calculated by Fairlie et al. (2010) off the coast of China. The contribution of nitrates on sea-salt is lower and generally close to 0.5 mg m^{-2} over the continents. It only reaches 1 mg m^{-2} in localized areas, in particular off the coast of the Eastern US, or over the Mediterranean where both pollution and sea-salt particle are present. This is somewhat in contrast with Myhre et al. (2006) who calculated a larger and more localized contribution of sea-salt to the total nitrate column over Northern Europe reaching more than 1–1.5 mg m^{-2}. The global mean burden of fine mode nitrate is 0.44 mg m^{-2}. Nitrates on dust and on sea-salt contribute respectively for 0.65 mg m^{-2} and 0.48 mg m^{-2} to the coarse nitrate global burden. This corresponds to a relative contribution of nitrate on pure sulfates of 28 % of the total nitrate burden in this model, to be compared to the 21 % calculated by Bauer et al. (2007) and to the 23 % calculated by Xu and Penner (2012).

As discussed in Sect. 2, the formation of fine nitrate particles depends on both the ammonia and nitric acid concentrations. Figure 6 shows the annual mean surface concentration of NH_3 and HNO_3. The concentration of ammonia reaches more than 1–2 µg m^{-3} where agricultural emissions are high, in particular over Northern Europe, in the central United States, in the Ganges valley and in Northern China. In Northern Europe, India, and China, the concentration reaches more than 5 µg m^{-3}. Biomass burning also contributes to higher concentrations in Indonesia, Africa, and South America. This distribution is very much in line with the column density measured by the IASI instrument (Clarisse et al., 2009) and a more detailed and quantitative evaluation of the NH_3 results with the remote sensing data will be presented in forthcoming studies. Nitric acid shows high concentrations of 3–5 µg m^{-3} in regions of high anthropogenic NO_x emissions. This is in particular the case over the Eastern United States and to a lesser extent in California. In Europe, the concentration reaches 1–2 µg m^{-3} with a marked maximum over the Mediterranean sea where pollution accumulates. A more detailed evaluation of nitric acid has been provided elsewhere (Hauglustaine et al., 2004; Fol-

ACPD
14, 6863–6949, 2014

berth et al., 2006), although in a model version without a particle formation loss term, which we estimate in budget calculations to be approximately one third, see below. These distributions are in very good agreement with the results shown for instance by Xu and Penner (2012). These calculated surface concentrations of nitrate precursors explain the distribution of fine nitrate particles illustrated in Fig. 1 and the region of formation where both NH_3 and HNO_3 concentrations are high. As illustrated by Xu et Penner (2012), Fig. 7 shows the free ammonia T_A^* to total nitrate T_N ratio. Regions with a negative ratio represent the regions where no excess ammonia is present either due to very low ammonia concentrations or high sulfates concentrations. In these regions all the ammonia is used to neutralize the sulfates and form ammonium sulfate. At the surface these regions are mostly encountered over the ocean or over the deserts and remote continental areas. Due to the short lifetime of ammonia (less than 1 day), these regions expand as altitude increases. In the middle troposphere, only small fine nitrate formation regions persist in convective and biomass burning areas subject to rapid upward transport of emissions. A ratio larger than 1 corresponds to regions where ammonia is abundant and hence the formation of nitrate is limited by the amount of nitric acid available. This condition is mostly met at the surface over regions with high ammonia concentrations, in Northern Europe, the central US, India, China and biomass burning regions. This is also the case over the ocean where natural oceanic NH_3 emissions are present in a low NO_x environment. In other regions ($0 < \text{ratio} < 1$), the formation of nitrate is limited by the amount of ammonia available. These results are in agreement with the findings of Xu and Penner (2012).

Table 2 gives the global budget of nitric acid and nitrate particles for both the "present-day" (2000) and "pre-industrial" (1850) conditions. A similar budget has been presented by Xu and Penner (2012) and we refer to their study for sake of comparison with our results. For the present, we calculate a total source of HNO_3 of 48.5 $\mathrm{Tg\,N\,yr^{-1}}$ mostly arising (44.6 $\mathrm{Tg\,N\,yr^{-1}}$) from the gas phase reaction of NO_2 with OH. The heterogeneous formation of HNO_3 from the reaction of N_2O_5 with sulfate aerosols contributes only 3.9 $\mathrm{Tg\,N\,yr^{-1}}$ (or 8 %) nitric acid. This is in contrast to Xu and Penner

ACPD
14, 6863–6949, 2014

(2012) who calculated a larger contribution of heterogeneous chemistry of 42 %. The reason for this disagreement is unclear. The total loss totals 49.5 Tg N yr^{-1}. The small unbalance between source and loss arises from the stratospheric input of nitric acid into the considered domain for this budget (up to 200 hPa). Dry and wet deposition contribute about equally (respectively 14.7 and 17.0 Tg N yr^{-1}) to the total nitric acid deposition loss representing more than 60 % of the total HNO_3 loss. The total loss through nitrate formation totals 14.4 Tg N yr^{-1}. Nitric acid photolysis and reaction with OH contribute for 3.4 Tg N yr^{-1}. These terms are in line with Xu and Penner (2012) with a larger contribution of dry deposition in LMDz-INCA. The HNO_3 tropospheric burden is 0.3 Tg N, a value similar to Xu and Penner (2012) and the burden lifetime (burden divided by total loss rate) is 2.25 days in this model to be compared to a burden lifetime of 2.59 days derived from their budget. The source of nitrates (14.4 Tg N yr^{-1}) is constituted as 22 % from the fine mode ammonium nitrate formation and the rest from the formation of coarse nitrates on dust and sea-salt. Most of the nitrate loss is ensured by wet deposition (12.7 Tg N yr^{-1}). We calculate a total nitrate burden of 0.18 Tg N with 28 % corresponding to the fine mode and the rest as coarse particles on dust and sea-salt. The corresponding lifetime is 4.61 days. The burden of NO_3^- in the troposphere has doubled since the pre-industrial and its lifetime has decreased from 6.75 days in the pre-industrial to its present-day value, reflecting the more efficient scavenging of accumulation mode nitrate particules.

Table 3 summarizes the global budget of ammonia and ammonium. The only source of NH_3 into the atmosphere is the surface emission totalizing 50.5 Tg N yr^{-1} for the present-day. The deposition of ammonia arises from dry (11.0 Tg N yr^{-1}) and wet deposition (21.3 Tg N yr^{-1}). The formation of ammonium sulfate and ammonium nitrate contributes for 17.5 Tg N yr^{-1} (35 %) to the total loss of NH_3. The gas phase chemistry oxidation of NH_3 contributes for a negligible amount to its loss. The burden of NH_3 has increased from 0.05 Tg N in the pre-industrial to 0.09 Tg N for the present-day. The corresponding present-day lifetime of ammonia in the atmosphere is 0.63 days. The only source of NH_4^+ is the ammonium sulfate and ammonium nitrate forma-

ACPD
14, 6863–6949, 2014

tion (17.5 Tg N yr^{-1}). The loss arises mostly from wet deposition (14.9 Tg N yr^{-1}) and to a lesser extent from surface dry deposition (2.5 Tg N yr^{-1}). The burden of NH_4^+ is 0.22 Tg N with a lifetime of 4.52 days in the atmosphere.

3.2 Surface deposition

In Fig. 8 we present the total (dry + wet) annual deposition of SO_x ($= SO_2 + SO_4^{2-}$), NH_x ($= NH_3 + NH_4^+$), and NO_y ($= NO + NO_2 + NO_3 + HNO_2 + HNO_3 + HNO_4 + 2N_2O_5$ + PAN + organic nitrates + particulate NO_3^-). The three plots show similar patterns with high deposition over Northern America, Europe, India and China. The total SO_x deposition is 107 Tg S yr^{-1} with wet deposition contributing for 75 % to this total. The maximum sulfur deposition reaches 5 g S m^{-2} yr^{-1} in Northern China. Over Northern America a maximum deposition reaching 1–2 g S m^{-2} yr^{-1} is calculated over the Eastern United States. In Western Europe, the deposition ranges from 500 mg S m^{-2} yr^{-1} in the South to about 2 g S m^{-2} yr^{-1} in the North, value reached over the UK. A maximum deposition reaching 2 g S m^{-2} yr^{-1} is calculated in central Europe. The global NH_x deposition is close to 50 Tg N yr^{-1} with wet and dry deposition contributing each for 50 % to this total (see Table 3). The total ammonia deposition reaches maximum values of 2–3 g N m^{-2} yr^{-1} over Northern Europe, Northern India and more than 5 g N m^{-2} yr^{-1} in China. Over Northern America, a maximum deposition reaching 800 mg N m^{-2} yr^{-1} is calculated over the central United States. The total oxidized nitrogen deposition totals 50 Tg N yr^{-1} with wet deposition contributing for 60 % to this term. Interestingly, total NH_x and total NO_y contribute for the same amount to the global nitrogen deposition to the surface ecosystems. The total NO_y deposition shows a slightly different pattern from the other deposition terms with a maximum reaching 1.5 g N m^{-2} yr^{-1} over the Eastern United States, Northern India and China. In Europe the NO_y deposition reaches 800–900 mg N m^{-2} yr^{-1}. These distributions are in good agreement with the total deposition illustrated by Dentener et al. (2006b) and resulting from the ensemble mean of 23 at-

ACPD
14, 6863–6949, 2014

mospheric models and with the distributions illustrated by Lamarque et al. (2013) for the ACCMIP simulations.

Figure 9 compares the wet deposition of these three terms calculated by the model with the measurements from the EMEP network over Europe, from the NADP network over Northern America and from the EANET network over Eastern Asia. These comparisons were prepared using the AEROCOM evaluation tools. The sulfate deposition is slightly underestimated by the model with a Normalized Mean Bias (NMB) of −27 % in Europe and −20 % in Northern America. In Eastern Asia, a higher underestimation is obtained (NMB = −60 %). A similar disagreement in Eastern Asia was also obtained by Dentener et al. (2006b) and by Lamarque et al. (2013) and tentatively attributed to unaccounted sources of SO_2 from coal burning in China. The wet deposition of NH_x is well represented in Europe (NMB = −4.5 %) and to a lesser extent in Northern America (NMB = −32 %). We note however that the deposition term is again significantly underestimated in Eastern Asia (NMB = −60 %). The wet deposition of oxidized nitrogen from $HNO_3 + NO_3^-$ is relatively well represented in Europe (r = 0.49) but underestimated by −28 %. Over Northern America, a better comparison is obtained (NMB = −13 %, r = 0.73). Again, in Eastern Asia, a significant underestimate of the wet deposition is obtained (NMB = −54 %). Work is underway in order to better understand the reason of the significant underestimate of the deposition terms in Eastern Asia and in particular in China based on new emission inventories generated for this region (Wang et al., 2012).

3.3 Aerosol optical properties and radiative forcings

The aerosol optical depth and direct radiative forcings of the various aerosol components are calculated on-line by the General Circulation Model. The solar radiation code in the LMDz GCM consists of an improved version of the parameterizations of Fouquart and Bonnel (1980). The shortwave spectrum is divided into two intervals: 0.25–0.68 µm and 0.68–4.00 µm. The model accounts for the diurnal cycle of solar radiation and allows fractional cloudiness to form in a grid box. The radiative fluxes are computed every

ACPD
14, 6863–6949, 2014

2 h, at the top of the atmosphere and at the surface, with and without the presence of clouds. The clear-sky and all-sky radiative forcings of the various aerosol components are finally obtained by subtracting the 1850 radiative fluxes from the considered simulation.

Figure 10 shows the calculated total aerosol optical depth at 550 nm and the optical depth associated with fine and coarse nitrate particles. The total aerosol optical depth (AOD) exhibits values of 0.15–0.25 over the Eastern United States and Europe associated mostly with pollution aerosols. Maximum values reaching more than 0.5 and associated with dust aerosols are calculated over Northern Africa, Arabia, and China. In China, both natural and pollution aerosols contribute to the high aerosol optical depth. Distributions very similar to these results have also been presented in other studies (e.g., Kinne et al., 2006; Bellouin et al., 2011; Xu and Penner, 2012; Shindell et al., 2013). The global mean and total AOD is 0.059. As expected from the burden shown in Fig. 2, nitrates exhibit higher optical depth over source regions: values of 0.02–0.03 over the central United States, and maximum optical depth of 0.05 in northern Europe and more than 0.1 in Northern China. The contribution of nitrates formed from biomass burning emissions is also visible in South America, Africa, and Indonesia with values reaching 0.1 in the later region. The nitrate optical depth is in good agreement with the results presented by Myhre et al. (2006) regarding both the general patterns of the distribution and the calculated values. The global mean and total nitrate optical depth is 0.0053. Fine nitrate particles contribute for 0.0048 to this total number. Figures 11 and 12 present an evaluation of the calculated total AOD by comparing with the measurements from the AERONET network (Holben et al., 2001; Kinne et al., 2006). Matching daily data from the model and Aeronet were aggregated to monthly averages. Worldwide (Fig. 11), the measured and modeled AOD show a relatively good correlation (R = 0.57). The arithmetic mean for the measurements of 0.226 is however underestimated by the modeled values of 0.202 with a Normalized Mean Bias (NMB) of −11 %. Figure 12, shows the evaluation with the AERONET measurements for various regions. A good agreement with the AERONET measurements is obtained over North-

ACPD
14, 6863–6949, 2014

ern America. Over this region the model slightly underestimates the measurements (NMB = −5 %, R = 0.77). Over Africa, higher AOD associated with dust aerosols are calculated. A fairly good correlation is reached (R = 0.66) with also a light underestimate by the model of −10 %. Over Eastern Asia, the model underestimate the AOD (NMB = −39 %). Over Europe, a similar correlation between model and measurement is obtained (R = 0.58). However, over this region, the model overestimates the measurements (NMB = +6 %).

Figure 13 shows the zonal nitrate column and the corresponding optical depth at 550 nm. These figures show both the fine and coarse mode components for the two variables. The total zonal mean nitrate aerosol column peaks in the Northern Hemisphere around 25–40° as shown already in Fig. 2. Coarse particles dominate the nitrate burden and reach 2.5 mg m^{-2}. These particles are also responsible for a background column of 0.5–0.8 mg m^{-2} in remote areas, associated mainly with coarse nitrate particles on sea-salt. Fine particles associated with pollution present a maximum of about 1 mg m^{-2} at 40° N and a secondary maximum of about 0.5 mg m^{-2} associated with biomass burning emissions around the equator. The zonal mean nitrate optical depth shows the opposite behavior since coarse particles contribute less efficiently to the Mie scattering. The total zonal mean nitrate optical depth reaches more than 1.2 around 40° N. This optical depth is largely associated with fine particles with coarse nitrates contributing for a maximum optical depth of about 0.2.

Figure 14 gives the direct radiative forcings of aerosols since pre-industrial times calculated at the top of the atmosphere for all-sky conditions. The forcings are calculated as the difference between the present-day and pre-industrial aerosol distributions. The sulfate radiative forcing is −0.315 W m^{-2} in global mean. A value in agreement with the recent intercomparison of models provided in the framework of AEROCOM by Myhre et al. (2013) indicating a mean forcing of -0.32 ± 0.11 W m^{-2} and with the most probable range of −0.18 to −0.44 W m^{-2} provided by Shindell et al. (2013). The forcing shows values of −2 W m^{-2} over regions of high sulfate load over the Eastern United States, Southern Europe and Eastern Asia. The radiative forcing associated

ACPD
14, 6863–6949, 2014

with Black Carbon (BC) particles including both the fossil fuel, biofuel and biomass burning components is equal to 0.19 $W m^{-2}$ in global mean. Over the Southeastern United states and the UK, the negative forcing indicates that BC emissions have decreased in these regions since the reference year of 1850 already included emissions from biofuel and to a lesser extent coal burning. The Organic Carbon (OC) forcing is $-0.056\,W m^{-2}$. The forcing is negative except in regions where emissions have decreased as mentioned for BC. Myhre et al. (2013) reported a radiative forcing arising from fossil fuel and biofuel BC of $+0.18 \pm 0.07\,W m^{-2}$, a forcing of $-0.03 \pm 0.01\,W m^{-2}$ for OC, and a combined BC + OC forcing from biomass burning of $-0.00 \pm 0.05\,W m^{-2}$. The calculated forcings for BC and OC with this model are in agreement with this compilation and with Shindell et al. (2013). The calculated global mean forcing for nitrate particles is $-0.056\,W m^{-2}$. Fine nitrate particules contribute for $-0.049\,W m^{-2}$ to this forcing and anthropogenic coarse nitrate particulate matter for only $-0.006\,W m^{-2}$. The total nitrate forcing reaches $-2.6\,W m^{-2}$ over China, $-1.0\,W m^{-2}$ over Northern Europe and $-0.5\,W m^{-2}$ over the central United States. The nitrate forcing also reaches more than $-1.0\,W m^{-2}$ over biomass burning regions. For this forcing, Myhre et al. (2013) reported a global value of $-0.08 \pm 0.04\,W m^{-2}$ and Shindell et al. (2013) a value of $-0.19 \pm 0.18\,W m^{-2}$. There is a significant spread in the calculated nitrate forcings from the various model ranging from a value of $-0.02\,W m^{-2}$ with the OsloCTM2 to $-0.12\,W m^{-2}$ with the GEOS-CHEM model (Myhre et al., 2013) and even to $-0.41\,W m^{-2}$ with the GISS model (Shindell et al., 2013). The value calculated with this model is in the range provided by this previous work. Additional work is required to understand the reason of the spread in the various model estimates.

4 Future evolution

In this section, we present the future evolution of nitrate aerosols under the various RCP scenarios for the 2030, 2050 and 2100 periods. The associated direct radiative forcings are presented and the nitrate forcing compared to the forcing of the other parti-

ACPD
14, 6863–6949, 2014

cles in order to investigate their relative contribution in the future. Snapshot simulations have been performed for these various cases as described in Sect. 2.3 and the global emissions for key species related to nitrate formation have been presented in Table 1. In order to better understand the contribution of NH_3, NO_x, and SO_2 emissions to the future nitrate levels, sensitivity simulations have been performed in the particular case of the RCP4.5 scenario for the year 2100.

4.1 Atmospheric composition

The four RCP scenarios have been simulated with the model but, as far as nitrate particles and their radiative forcing are concerned, and as visible from the total emissions presented in Table 1, two particular scenarios are interesting to compare. In all scenarios, SO_2 and BC emissions decrease from their present day value to their 2100 level. Despite significant differences in 2030 and 2050 (in particular in the case of SO_2 emissions), the level reached in 2100 for the four emission scenarios are often close to each other for these species. This is not the case for two important precursors of nitrate particles: ammonia and nitrogen oxides. For NH_3 and NO_x, RCP4.5 and RCP8.5 represent the extremes for emissions in 2100 and are expected to lead to very different nitrate levels in the future. This is in particular the case for NH_3 emissions, which remain close to their present-day level (51 Tg N) in 2100 for the RCP4.5 scenario (54 Tg N), but increase by 50 % in 2100 for RCP8.5 (78 Tg N). For NO_x, emissions decrease from 46 Tg N for the present-day to 24 Tg N in 2100 for RCP4.5 but decrease only to 31 Tg N in 2100 for RCP8.5.

As a consequence of these changes in emissions, the concentration of NH_3 varies quite significantly in the future between these two extreme scenarios. Figure 15 shows the change in NH_3 surface concentration from the present-day levels in 2030 and 2100 for both RCP4.5 and RCP8.5 (see Fig. 6 for the reference level). For RCP8.5 a significant increase is calculated everywhere in 2030 and 2100 except in Indonesia where biomass burning emissions are reduced. In the central United States, Northern and central Europe, India and China, NH_3 increases by up to 2 $\mu g\,cm^{-3}$ in 2100.

ACPD
14, 6863–6949, 2014

For the RCP4.5 scenario, a significant increase is still predicted in India and in China where emissions are still predicted to rise. However, concentrations are significantly reduced in Western and Eastern Europe by up to 1 $\mu g\,cm^{-3}$ and a lesser increase of 0.5–1 $\mu g\,cm^{-3}$ is calculated in the central US. Figure 16 shows the corresponding change in HNO_3 surface concentrations. Due to a reduction in NO_x emissions, HNO_3 has already significantly decreased in 2030 in Northern America and Europe in both scenarios. In contrast, a strong increase is calculated in India and in China reaching more than 2 $\mu g\,cm^{-3}$ in 2030. In 2100, the HNO_3 reduction is almost generalized over the continents with the exception of biomass burning regions in Africa and India in the case of RCP8.5. Figure 17 shows the change in SO_4^{2-} surface concentration in 2030 and 2100 for RCP8.5. The concentration increases in India and Southeast Asia by more than 2 $\mu g\,cm^{-3}$ in 2030. As expected from the sharp decrease in SO_2 emissions, at the end of the XXIst century, a general decrease of the surface concentration is calculated, reaching more than 2 $\mu g\,cm^{-3}$ in Northern America, Europe, and China.

As a result of these changes in nitrate precursor surface concentrations, nitrate particles are expected to undergo significant variations in the future. Figure 18, shows the evolution of nitrate particles surface concentrations for the various simulations performed and averaged over several regions of the world. As shown earlier (Fig. 1), present-day nitrate concentrations are higher in Europe (1.4 $\mu g\,cm^{-3}$) than in Northern America (0.35 $\mu g\,cm^{-3}$). Due to the decrease in precursors, the concentrations in these two regions decrease for all scenarios during the XXIst century. By 2100, the mean surface concentration in Europe is in the range 0.14–0.43 $\mu g\,cm^{-3}$ and in the range 0.03–0.15 $\mu g\,cm^{-3}$ in northern America. In northern and southern Asia, the concentration increases significantly in 2030 and 2050 in scenarios RCP6.0 and RCP8.5 reaching 3.6 $\mu g\,cm^{-3}$. By 2100, the surface concentration is in the range 0.38–0.78 $\mu g\,cm^{-3}$ and 0.01–0.51 $\mu g\,cm^{-3}$ in northern and southern Asia, respectively. In India, the surface nitrate concentration increases until 2050 in most scenarios, reaching 1.45 $\mu g\,cm^{-3}$ on average. The concentration then decreases and is in the range 0.27–0.65 $\mu g\,cm^{-3}$ in 2100. The concentration of nitrates in other regions (Africa, South America, Australia)

ACPD
14, 6863–6949, 2014

show little variation from their present-day value (not shown). The global nitrate concentration increases from 0.38 $\mu g\,cm^{-3}$ for the present to 0.58 $\mu g\,cm^{-3}$ in 2030 and decreases to 0.10–0.21 $\mu g\,cm^{-3}$ in 2100.

Figure 19 shows the free ammonia (T_A^*) to total nitrate ratio (T_N) for the year 2100 and scenario RCP8.5. There is a significant increase in this ratio at the surface and in the free troposphere compared to the reference simulation (Fig. 7). At the surface, negative ratios indicating the formation of ammonium sulfate instead of ammonium nitrate have vanished over the continents due to a significant and general reduction in SO_4^{2-} concentrations. The ratio has also increased over the continents to values generally larger than 1, indicating an increased excess of ammonia over nitric acid, and a stronger limitation of particle formation by HNO_3 concentrations. This is a direct consequence of lower HNO_3 and higher NH_3 concentrations in 2100. Interestingly, in the free troposphere, the T_A^*/T_N ratio becomes positive in the Northern Hemisphere due to the decreased sulfate concentrations. As a consequence nitrate particles will form at higher altitudes, mostly limited by the amount of NH_3 present at these altitudes.

Figure 20, shows the change from the present-day (Fig. 4) of the nitrate column in 2030 and 2100 for the two extremes scenarios RCP4.5 and RCP8.5. As discussed above, the change in nitrate precursors is responsible for a strong increase of the nitrate column in the Northern Hemisphere of 1–2 $mg\,m^{-2}$ on average and reaching up 2–5 $mg\,m^{-2}$ in the case of RCP8.5, in 2100. In the case of RCP4.5, the column increases by 0.4–0.8 $mg\,m^{-2}$ in the Northern Hemisphere with a maximum of 1–2 $mg\,m^{-2}$ over India. In all cases and in both 2030 and 2100, a strong increase in the nitrate column is calculated over India. In both scenarios, the strong decrease in nitrate surface concentrations calculated over Europe and China in 2030 and 2100 (Fig. 18) dominates the change in the column which decreases by up to 2 $mg\,m^{-2}$ over these regions. In the case of RCP4.5, this is also the case over the central US with a decrease reaching 0.4 $mg\,m^{-2}$. For scenario RCP8.5, in 2100, it is interesting to note that the nitrate column also increases in the Southern Hemisphere by 0.1–0.4 $mg\,m^{-2}$ mostly associated with transport from source regions in Africa and South America.

ACPD
14, 6863–6949, 2014

Figure 21 and Table 4 present the evolution in the global burden of nitrate particles and its main precursors for the various scenarios and time-slice experiments. In all scenarios, the burden of fine nitrate particles increases in the atmosphere from a present-day value of 0.05 Tg N to 0.13 Tg N for RCP8.5 and 0.07 Tg N for RCP4.5. As expected, these two extreme values are mainly driven by the change in NH_3 emissions and burden. The burden of NH_3 increases from its present-day value of 0.09 Tg N to a maximum value of 0.23 Tg N in 2100 in the case of RCP8.5 and to a minimum value of 0.14 Tg N for RCP4.5. The formation of coarse nitrate on dust and sea-salt is a result of HNO_3 heterogeneous uptake on these particles. Since no change in climate is considered in these simulations, the burden of dust and sea-salt particles is similar in all simulations. Therefore, the evolution of the coarse nitrate particle burden follows the evolution of the nitric acid in the atmosphere, and decreases from 0.13 Tg N to 0.09–0.12 Tg N in 2100. Overall, the burden of total nitrate particles increases from 0.181 Tg N to 0.183 Tg N in 2100 in the case of RCP4.5 and to 0.247 Tg N in the case of RCP8.5. The relative contribution of fine particles to this total is however modified and increased from a present-day value 28 % to 40 % in 2100 for RCP4.5 and to 51 % for RCP8.5. Since fine particles contribute the most to the nitrate optical depth and radiative forcing this feature will have consequences on the climate impact of these particles. The future decrease in sulfates leading less ammonium sulfate formation is partially compensated by an increase in ammonia and formation of ammonium nitrate. As a consequence, the NH_4^+ global burden remains fairly constant in time and varies from a present-day value of 0.21 Tg N to 0.17–0.24 Tg N in 2100.

4.2 Sensitivity to NH_3, NO_x, and SO_2 emissions

As discussed earlier, as a direct consequence of future changes in nitrate precursors, scenarios RCP8.5 and RCP4.5 represent the two extremes as far as future nitrates concentrations are concerned. Indeed, SO_2 emissions are close in both scenarios but NO_x and to a larger extent NH_3 emissions are significantly different and at the extremes of their future evolution. Three sensitivity experiments have been performed in order to

ACPD
14, 6863–6949, 2014

investigate the relative importance of these emissions on the future nitrate levels. These sensitivity studies have been derived from scenario RCP4.5 for 2100 in order to better understand the role played by SO_2, NO_x and NH_3 emissions on the differences obtained between RCP4.5 and RCP8.5 (see Table 1). Simulation 2100 RCP4.5-NO_x has the same emissions as scenario RCP4.5 except that the NO_x emissions are replaced by 2100 RCP8.5 emissions. Similarly in simulation 2100 RCP4.5-NH_3 all emissions are similar to RCP4.5 except that the NH_3 emissions are replaced by 2100 RCP8.5 emissions. Finally, in simulation 2100 RCP4.5-SO_2 all emissions are similar to RCP4.5 except that SO_2 emissions are replaced by 2000 emissions. The latter are chosen to come not from the rather similar RCP8.5, and to isolate the impact of sulfates.

Figure 21 and Table 4 summarize the impact of these sensitivity simulations on the global burden of nitrates and related species in 2100. When NH_3 emissions are increased to their RCP8.5 level (RCP4.5-NH_3) the burden of NH_3 increases to 0.24 Tg N, a value even larger than in scenario RCP8.5. In this case, the fine nitrate burden increases to 0.12 Tg N, showing that more than 80 % of the difference in fine nitrates between RCP4.5 and RCP8.5 can be explained by the higher NH_3 emissions in scenario RCP8.5. In this case, more ammonium nitrate is formed, and the NH_4^+ burden increases to 0.22 Tg N, a value slightly below the RCP8.5 scenario. This can be explained by the fact that less nitric acid is present in RCP4.5 compared to RCP8.5 and hence less ammonium nitrate is formed since HNO_3 is the limiting species as seen in Fig. 19. Since ammonium sulfates form on preexisting SO_4^{2-} particles, changing the NH_3 emissions has no effect on the sulfates themselves in this sensitivity simulation. The impact of somewhat higher NO_x emissions (simulation RCP4.5-NO_x), increases the nitric acid burden to a value close to their RCP8.5 level. As a result, the fine nitrate burden increases by 0.01 Tg N, explaining the remaining difference obtained between RCP4.5 and RCP8.5 scenarios. These sensitivity simulations show that the strong difference calculated in fine nitrate particle levels in 2100 between scenario RCP4.5 and RCP8.5 can be explained mostly (80 %) by the higher NH_3 emissions in the case of RCP8.5 and the remaining explained by the higher NO_x emissions. Finally, we illustrate the

ACPD
14, 6863–6949, 2014

impact of higher SO_2 emissions in the system (simulation RCP4.5-SO_2). In this case, since 2000 emissions have been used, as expected the SO_4^{2-} burden increases to the present-day value. As a consequence, more NH_3 is used to neutralize the sulfates and form ammonium sulfates in priority, and the fine nitrate burden decreases by 0.02 Tg N.

4.3 Surface deposition

Figure 22 shows the evolution of the total nitrogen deposition averaged over various regions of the world. The total $NO_y + NH_x$ (wet + dry) deposition is presented. In Europe and Northern America, the total N deposition slightly decreases or remains close to its present-day value in the case of scenario RCP8.5. In these regions, the NO_y deposition significantly decreases in the future due to reduced NO_x emissions (from 360 mg N m^{-2} yr^{-1} to 88–150 mg N m^{-2} yr^{-1} in Europe in 2100 and from 265 mg N m^{-2} yr^{-1} to 60–108 mg N m^{-2} yr^{-1} in Northern America). However, this decrease is largely compensated by an increase in NH_x deposition. In Europe for instance, this term increases from 426 mg N m^{-2} yr^{-1} to 672 mg N m^{-2} yr^{-1} in 2100 for RCP8.5. As a consequence, the fraction of N deposited as NH_x increases from about 50 % for the present-day to 70–80 % in 2100 in these two regions (Fig. 23). In Asia and India, the NO_y deposition generally increases in 2030 or 2050 due to higher NO_x emissions in these regions before decreasing at the end of the XXIst century. In addition, the NH_x deposition generally increases during the course of the century to reach maximum values in 2100. As a result, the total N deposition generally reaches a maximum in 2030–2050 and further increases or remains stable until 2100. In Northern Asia (mostly China) for instance, the total deposition increases from 965 mg N m^{-2} yr^{-1} for the present to up to 1443 mg N m^{-2} yr^{-1} in 2050 before decreasing to 880–1251 mg N m^{-2} yr^{-1} in 2100. In India, the deposition increases during the century from a present-day value of 780 mg N m^{-2} yr^{-1} to 1100–1700 mg N m^{-2} yr^{-1} in 2100. As seen in other regions, this increase in total N deposition is also associated with a new balance between NO_y and NH_x deposition. As seen from Fig. 23, the frac-

ACPD
14, 6863–6949, 2014

tion of N deposited as NH_x increases from about 60 % to 80 % in these regions. The same tendency is found over oceanic regions and globally. The total N deposited remains fairly stable or slightly decreases in these regions during the XXIst century but the fraction of N deposited as NH_x increases from 45 % to 55–70 % over the ocean and from 55 % to 70–80 % globally. This feature has possible strong consequences for terrestrial or oceanic ecosystems because as nitric acid, which dissociates readily in water causing a significant drop in pH, deposition in the form of NH_x in contrast increases the water alkalinity (Doney et al., 2007).

4.4 Anthropogenic aerosol optical depths and radiative forcings

Table 5 gives the anthropogenic aerosol optical depth at 550 nm for the various aerosol components and for the different performed simulations. As in Bellouin et al. (2011), we define the anthropogenic optical depth by substracting the optical depth calculated in 1850 to the calculated value. The total anthropogenic optical depth decreases in all scenarios from a present-day value of 0.027 to a range of 0.009 for RCP4.5 to 0.016 for RCP6.0 and RCP8.5 in 2100. The anthropogenic optical depth of all aerosols decreases from 2000 to 2100 for all scenarios except for nitrates for which the optical depth increases in all RCP storylines. The nitrate optical depth increases from 0.004 in 2000 to a range in 2100 of 0.005 for RCP4.5 to 0.009 for RCP8.5. Figure 24 summarizes the contributions of the various aerosol components to this total anthropogenic optical depth. For the present-day, sulfates have the largest contribution of 64 %. OC and BC contribute respectively for 19 % and 5 % to the anthropogenic optical depth. Nitrates have a contribution of 13 %. In the future, the contribution of sulfate decreases for all scenarios to a range of 16 % in the case of RCP2.6 to 36 % for RCP4.5 in 2100. The contribution of BC in 2100 ranges from 3 % for RCP2.6 to 5 % in RCP6.0 and the contribution of OC from 3 % in RCP4.5 to 30 % in RCP6.0. In all scenarios, we calculate an increasing contribution of nitrates to the anthropogenic aerosol optical depth, and in 2100, nitrates become the dominant contributors to the anthropogenic optical depth. This contribution in 2100 ranges from 46 % for RCP6.0 to 64 % in RCP2.6.

ACPD
14, 6863–6949, 2014

Table 6 gives the all-sky direct radiative forcings since 1850 at the Top Of the Atmosphere (TOA) of the various aerosol components calculated for the different scenarios and time periods. The total forcing decreases from a present-value of $-0.23\,W\,m^{-2}$ to -0.11, -0.07, -0.11 and -0.13 for scenarios RCP2.6, 4.5, 6.0 and 8.5, respectively. The geographical distribution of the total direct forcing for scenario RCP8.5 is shown in Fig. 25. In 2000, the forcing is strongly dominated by the negative sulfate forcing in the Northern Hemisphere with negative values over the continents reaching $-6\,W\,m^{-2}$ in China. The positive forcing associated with BC dominates in several areas, in particular in the tropics, in biomass burning regions, or over regions with high surface albedo (see also Fig. 14 for the individual aerosol forcings in 2000). In 2100, the negative total forcing decreases but remains negative over most of the Northern Hemisphere. The maximum negative forcings are calculated over the central US where the nitrate forcing is high, over India and China. In these regions, the negative forcing reaches $-1.6\,W\,m^{-2}$. The positive forcing also decreases, except over the southeastern United States due to decreasing emissions of OC since 1850.

Figure 26 shows the evolution of the radiative forcings associated with the various aerosol components for the different RCP scenarios. As discussed above, the total aerosol forcing decreases from 2000 to 2100 for all scenarios. The negative forcing associated with sulfates decreases from $-0.31\,W\,m^{-2}$ in 2000 to a range of $-0.03\,W\,m^{-2}$ in RCP 2.6 to $-0.08\,W\,m^{-2}$ for RCP8.5. Similarly, the forcing arising from OC decreases from $-0.06\,W\,m^{-2}$ in 2000 to $-0.03\,W\,m^{-2}$ in 2100 for RCP4.5 and to $-0.05\,W\,m^{-2}$ for RCP6.0. In addition, the positive forcing associated with BC decreases from $0.19\,W\,m^{-2}$ in 2000 to 0.04–$0.10\,W\,m^{-2}$ in 2100. In contrast, to the other aerosol components, the nitrate negative forcing increases in all scenarios from a present-day value of $-0.05\,W\,m^{-2}$ to a value ranging in 2100 from $-0.06\,W\,m^{-2}$ for RCP4.5 to $-0.11\,W\,m^{-2}$ for RCP8.5.

Finally, Fig. 27 summarizes the impact of nitrates on the future evolution of the anthropogenic AOD at 550 nm and on the direct radiative forcing of aerosols at the top of the atmosphere. This figure can be compared to the results shown by Bellouin

ACPD
14, 6863–6949, 2014

et al. (2011). As indicated before, the anthropogenic aerosol optical depth generally decreases for all scenarios. Nitrates have an increasing contribution to this AOD and their contribution increases the AOD in 2100 from a factor of 1.8 for RCP6.0 to a factor of 2.8 for RCP2.6. These results are similar to Bellouin et al. (2011) who calculated a ratio for the AOD with and without nitrates of 2 in the case of RCP6.0 and 3.3 in the case of RCP2.6. The total aerosol forcing significantly decreases for all scenarios as a consequence of emission reduction for the main aerosols and aerosol precursors. In contrast, we have seen that the negative nitrate forcing increases in the future for all scenarios due to higher emissions of NH_3 from agriculture. Including nitrates in the radiative forcing calculations significantly increases the total direct forcing of aerosols by a factor of 1.3 in 2000, by a factor of 1.7–2.6 in 2030, by 1.9–4.8 in 2050, and by 6.4–8.6 in 2100. These ratios are larger than Bellouin et al. (2011) who included the first indirect effect in the aerosol forcing. These results show that due to increasing NH_3 emissions from agriculture in the future, nitrates have the potential to maintain the aerosol forcing at significantly higher values than those expected without including them in the climate simulations and become the main agent contributing to this forcing.

5 Conclusion

In this paper, the ammonia cycle and nitrate particle heterogeneous formation have been introduced in the LMDz-INCA global model. The model treats ammonia and nitrates interactively with the full tropospheric chemistry and the other types of aerosols. We consider both fine nitrate particles formation in the accumulation mode from nitric acid and ammonia reaction and coarse nitrate particles forming on existing dust and sea-salt particles. The model developed in this work reproduces distributions of nitrates and related species in agreement with previous pioneering studies. The present-day surface concentrations of sulfates, nitrates, and ammonium have been evaluated by comparison against network measurements from the EBAS database. In Europe and Northern America, the model captures the sulfates measurements with a mean bias

ACPD
14, 6863–6949, 2014

of about 20 %. As obtained with other models, ammonium and nitrates particles are more difficult to reproduce and higher biases are obtained, reaching, for nitrates, 50 % and 100 % over Europe and Northern America, respectively. The model total sulfate, ammonia, and nitrate deposition have also been compared to network measurements. This evaluation shows a reasonable agreement over Europe and Northern America for these three terms, with mean biases of about 20–30 % or better. This is not the case in Eastern Asia where systematically underestimated depositions are calculated. This points to the need to further improve the emission inventories in this region and in China in particular. The calculated total aerosol optical depth distribution is generally well reproduced by the model with a mean bias against the AERONET observations of 30 %.

The main objective of this work is to investigate the direct radiative forcing of climate of fine and coarse nitrate particles for both present-day and future conditions and investigate their relative contribution to the total aerosol forcing. Fine nitrate particles represent less than 30 % of the total nitrate burden. Nitrates contribute for 13 % to the anthropogenic AOD since the pre-industrial (1850). The calculated present-day total nitrate direct radiative forcing since the pre-industrial at the top of the atmosphere is $-0.056\,\mathrm{W\,m^{-2}}$. Despite their small contribution to the total nitrate burden, fine particles largely dominate the nitrate forcing representing close to 90 % of this forcing. The present-day nitrate direct radiative forcing has the same magnitude than the forcing associated with organic carbon particles and represent 18 % of the sulfate forcing. The nitrate forcing is subject to a significant spread in the previous model estimates. The forcing calculated with this model is within the range of -0.03 to $-0.17\,\mathrm{W\,m^{-2}}$ reported by Myhre et al. (2013) but in the lower range of this multi-model estimate.

The model has been used to investigate the future changes in nitrate concentration and direct radiative forcing of climate based on the four RCP scenarios and for the 2030, 2050 and 2100 time horizons. Due to a decrease in fossil fuel emissions in the future, the concentration of most of the species involved in the nitrate-ammonium-sulfate system drop by 2100 under the different scenarios. This is not the case for

ACPD
14, 6863–6949, 2014

ammonia which originates from agricultural practices and for which emissions significantly increase in the future. As a consequence, NH_3 future concentrations significantly increase in India, in Eastern Asia, and in Northern America for the four scenarios, but also in Europe for the most extreme scenario RCP8.5. Despite this increase in NH_3 surface levels, the surface concentration of nitrates decreases in Europe and Northern America due a significant reduction in NO_x and hence HNO_3 concentration at the surface. In other regions (India, Asia), the nitrate surface concentration generally increases until 2030–2050 due to increasing NO_x and NH_3 and then decrease until 2100. Due to the significant reduction in SO_4^{2-} levels in the future and concomitant increase in NH_3, large regions of the atmosphere, not only at the surface but also in the free troposphere, shift from an ammonium sulfate to an ammonium nitrate formation regime. As a consequence, despite the decrease of nitrates at the surface level in several regions, the global burden of accumulation mode nitrates in the atmosphere increases by a factor of 1.4–2.6 in 2100 depending on the scenario. This range is associated for 80 % to the range in future NH_3 emissions among the various scenarios with NO_x emissions contributing to the remaining variability between the different scenarios. The total nitrogen ($NH_x + NO_y$) deposition generally increases or remains fairly stable in the future for the different scenarios. However this feature is mostly associated with a decrease in NO_y deposition and an increase in NH_x deposition. As a consequence the fraction of nitrogen deposited as NH_x increases from about 50 % for the present-day to 70–80 % by 2100. This feature has possible strong consequences for the environment because as nitric acid causes a significant drop in pH, NH_x in contrast, increases the water alkalinity.

The total anthropogenic AOD decreases in all scenarios from a present-day value of 0.027 to a range of 0.009 for RCP4.5 to 0.016 for RCP6.0 and RCP8.5 in 2100. Since all aerosols concentrations decrease in the future except for nitrates, they become the dominant contributors to the anthropogenic AOD. Their contribution increases from 13 % for the present-day to 46–64 % in 2100 depending on the considered scenario. The total aerosol direct forcing decreases from its present-day value of $-0.23\,W\,m^{-2}$ to

ACPD
14, 6863–6949, 2014

−0.07 to −0.13 W m^{-2} in 2100 based on the considered scenario. As expected from the changes in the AOD, the direct forcing decreases for all aerosols in the future except for nitrates for which the direct negative forcing increases from −0.056 W m^{-2} in 2000 to a range of −0.060 to −0.115 W m^{-2} in 2100. Including nitrates in the radiative forcing calculations significantly increases the total direct forcing of aerosols by a factor of 1.3 in 2000, by a factor of 1.7–2.6 in 2030, by 1.9–4.8 in 2050 and by 6.4–8.6 in 2100. These results indicate and confirm that, due to increasing NH_3 agricultural emissions in the future according to the RCP emission scenarios, nitrates become the dominant contributor to the anthropogenic aerosol optical depth during the second half of the XXIst century and significantly increase the calculated aerosol direct forcing.

Agricultural emissions of ammonia are found to play a key role in the future mitigation of climate change. It is found in this study that ammonium nitrate particles become the dominant contributor to the future direct forcing of aerosols. In addition, in terms of regional air quality, we have shown that nitrate levels at the surface are also significantly affected by future emissions of nitrate precursors with consequences on Particulate Matter levels in Northern America, Europe and Asia, and hence health impact. The future ammonia emissions also affect the total nitrogen deposited at the surface with possible consequences on land and ocean ecosystems. We note however that significant uncertainties remain in our simulations of future nitrate levels. The ammonium-nitrate-sulfate chemistry module used in this study has been designed for long-term coupled climate-chemistry simulations and remains relatively simple compared to the work of Metzger et al. (2002) and Xu and Penner (2012). This module could be improved in a future version of the model. We note however, the agreement with previous studies in terms of simulated distributions or in terms of comparison with measurements. No particular biases were obtained compared to these previous calculations. Another important limitation arises from the fact that in this study we analyze the role of future emissions acting separately on atmospheric composition. The impact of future climate change on nitrate formation or on dynamical regimes, on future levels of oxidants, on future biogenic emissions has not been considered. This will be investigated in forth-

ACPD
14, 6863–6949, 2014

coming studies along with the impact of nitrate particles on the aerosol indirect effect. It should also be noted that this study is based on the RCP scenarios for the future evolution of surface emissions of pollutants. All RCP scenarios assume aggressive air pollution abatement measures and this assumption is a major caveat in the projections of future nitrate precursor emissions. In addition, the small range of possible air pollutant emission trajectories across the RCPs may not necessarily be representative of the true regional air quality legislation and hence emission pathways. This type of study needs to be investigated with more realistic emission scenarios for air pollutants when they become available.

As stressed in this work and previous studies before, nitrate is an increasingly important aerosol component which impacts climate, air quality, and ecosystems through nitrogen deposition. Nevertheless, despite this importance for future climate and air quality projections, and unlike other aerosol components, the simulation of nitrate particles from global models and their impact on climate has not yet been extensively evaluated. Such an evaluation in the framework of the AeroCom community effort (Schulz et al., 2006; Myhre et al., 2013) will be of great interest to reduce the uncertainty on this aerosol component.

Acknowledgements. This study was co-funded by the European Commission under the EU Seventh Research Framework Programme (ECLAIRE and COMBINE projects) and by ADEME under the ACHIA project. D. A. Hauglustaine is grateful to J.-F. Lamarque for his assistance with the revised ammonia anthropogenic emissions. We thank A. Cozic for her continuous support with the LMDz-INCA model development. This work was performed using DSM-CCRT resources under the GENCI (Grand Equipement National de Calcul Intensif) computer time allocation. We are grateful to the numerous data providers of surface concentrations and deposition in the various networks (EMEP, NADP, IMPROVE, EANET). Essential is also the provision of the EBAS database extracts for model evaluation from NILU by P. Eckhardt, and help from J. Griesfeller in preparing these data for the AeroCom tools, which is supported by the EU ACTRIS project and EMEP.

ACPD
14, 6863–6949, 2014

References

Ackermann, I. J., Hass, H., Memmesheimer, M., Ziegenbein, C., and Ebel, A.: The parameterization of the sulfate-nitrate-ammonia aerosol system in the long-range transport model EURAD, Meteorol. Atmos. Phys., 57, 101–114, 1995.

Adams, P. J., Seinfeld, J. H., and Koch, D. M.: Global concentrations of tropospheric sulfate, nitrate, and ammonium aerosol simulated in a general circulation model, J. Geophys. Res., 104, 13791–13823, 1999.

Adams, P. J., Seinfeld, J. H., Koch, D., Mickley, L., and Jacob, D.: General circulation model assessment of direct radiative forcing by the sulfate–nitrate–ammonium–water inorganic aerosol system, J. Geophys. Res., 106, 1097–1112, doi:10.1029/2000JD900512, 2001.

Balkanski, Y.: L'Influence des Aérosols sur le Climat, Thèse d'Habilitation à Diriger des Recherches, Université de Versailles Saint-Quentin, Saint-Quentin-en-Yvelines, France, 2011.

Bauer, S. E., Balkanski, Y., Schulz, M., Hauglustaine, D. A., and Dentener, F.: Global modeling of heterogeneous chemistry on mineral aerosol surfaces: influence on tropospheric ozone chemistry and comparison to observations, J. Geophys. Res., 109, D02304, doi:10.1029/2003JD003868, 2004.

Bauer, S. E., Koch, D., Unger, N., Metzger, S. M., Shindell, D. T., and Streets, D. G.: Nitrate aerosols today and in 2030: a global simulation including aerosols and tropospheric ozone, Atmos. Chem. Phys., 7, 5043–5059, doi:10.5194/acp-7-5043-2007, 2007.

Bellouin, N., Rae, J., Jones, A., Johnson, C., Haywood, J., and Boucher, O.: Aerosol forcing in the climate model intercomparison project (CMIP5) simulations by the HadGEM2-ES and the role of ammonium nitrate, J. Geophys. Res., 16, D20206, doi:10.1029/2011JD016074, 2011.

Bouwman, A. F., Lee, D. S., Asman, W. A. H., Dentener, F. J., Van Der Hoek, K. W., and Olivier, J. G. J.: A global high-resolution emission inventory for ammonia, Global Biogeochem. Cy., 11, 561–587, 1997.

Brunner, D., Staehelin, J., Rogers, H. L., Köhler, M. O., Pyle, J. A., Hauglustaine, D., Jourdain, L., Berntsen, T. K., Gauss, M., Isaksen, I. S. A., Meijer, E., van Velthoven, P., Pitari, G., Mancini, E., Grewe, G., and Sausen, R.: An evaluation of the performance of chemistry transport models by comparison with research aircraft observations. Part 1: Concepts and

ACPD
14, 6863–6949, 2014

overall model performance, Atmos. Chem. Phys., 3, 1609–1631, doi:10.5194/acp-3-1609-2003, 2003.
Chin, M., Ginoux, P., Kinne, S., Holben, B. N., Duncan, B. N., Martin, R. V., Logan, J. A., Higurashi, A., and Nakajima, T.: Tropospheric aerosol optical thickness from the GOCART Model and comparisons with satellite and sun photometer measurements, J. Atmos. Sci., 59, 461–483, 2002.
Chung, S. H. and Seinfeld, J. H.: Global distribution and climate forcing of carbonaceous aerosols, J. Geophys. Res., 107, 4407, doi:10.1029/2001JD001397, 2002.
Claquin, T., Schulz, M., and Balkanski, Y. J.: Modeling the mineralogy of atmospheric dust source, J. Geophys. Res., 104, 22243–22256, 1999.
Clarisse, L., Clerbaux, C., Dentener, F., Hurtmans, D., and Coheur, P.-F.: Global ammonia distribution derived from infrared satellite observations, Nat. Geosci., 2, 479–483, 2009.
Cooke, W. F. and Wilson, J. J. N.: A global black carbon aerosol model, J. Geophys. Res., 101, 19395–19409, 1996.
Dentener, F. J. and Crutzen, P. J.: Reaction of N_2O_5 on tropospheric aerosols: impact on the global distributions of NO_x, O_3, and OH, J. Geophys. Res., 98, 7149–7163, 1993.
Dentener, F., Kinne, S., Bond, T., Boucher, O., Cofala, J., Generoso, S., Ginoux, P., Gong, S., Hoelzemann, J. J., Ito, A., Marelli, L., Penner, J. E., Putaud, J.-P., Textor, C., Schulz, M., van der Werf, G. R., and Wilson, J.: Emissions of primary aerosol and precursor gases in the years 2000 and 1750 prescribed data-sets for AeroCom, Atmos. Chem. Phys., 6, 4321–4344, doi:10.5194/acp-6-4321-2006, 2006a.
Dentener, F., Stevenson, D., Drevet, J., Lamarque, J.-F., Bey, I., Eickhout, B., Fiore, A., Hauglustaine, D., Horrowitz, L., Krol, M., Kuhlsherestha, U., Lawrence, M.,Galy-Lacaux, C., Rast, S., Shindell, D., Stevenson, D., Van Noije, T., Atherthon, C., Bell, N., Bergman, D., Butler, T., Cofala, J., Collins, W., Doherty, R., Ellingsen, K., Galloway, J., Gauss, M., Montanaro, V., Muller, J.-F., Pitari, G., Rodriquez, J., Sanderson, M., Strahan, S., Schultz, M., Sudo, K., Szopa, S., and Wild, O.: Nitrogen and sulfur deposition on regional and global scales: a multimodel evaluation, Global Biogeochem. Cy., 20, GB4003, doi:10.1029/2005GB002672, 2006b.
Doney, S. C., Mahowald, N., Lima, I., Feely, R. A., Mackenzie, F. T., Lamarque, J.-F., and Rasch, P. J.: Impact of anthropogenic atmospheric nitrogen and sulfur deposition on ocean acidification and the inorganic carbon system, P. Natl. Acad. Sci. USA, 104, 14580–14585, doi:10.1073/pnas.0702218104, 2007.

ACPD
14, 6863–6949, 2014

Dufour, G., Szopa, S., Hauglustaine, D. A., Boone, C. D., Rinsland, C. P., and Bernath, P. F.: The influence of biogenic emissions on upper-tropospheric methanol as revealed from space, Atmos. Chem. Phys., 7, 6119–6129, doi:10.5194/acp-7-6119-2007, 2007.

Emanuel, K. A.: A scheme for representing cumulus convection in large-scale models, J. Atmos. Sci., 48, 2313–2335, 1991.

Evans, M. J. and Jacob, D. J.: Impact of new laboratory studies of N_2O_5 hydrolysis on global model budgets of tropospheric nitrogen oxides, ozone, and OH, Geophys. Res. Lett., 32, L09813, doi:10.1029/2005GL022469, 2005.

Fairlie, T. D., Jacob, D. J., Dibb, J. E., Alexander, B., Avery, M. A., van Donkelaar, A., and Zhang, L.: Impact of mineral dust on nitrate, sulfate, and ozone in transpacific Asian pollution plumes, Atmos. Chem. Phys., 10, 3999–4012, doi:10.5194/acp-10-3999-2010, 2010.

Feng, Y. and Penner, J. E.: Global modeling of nitrate and ammonium: interaction of aerosols and tropospheric chemistry, J. Geophys. Res., 112, D01304, doi:10.1029/2005JD006404, 2007.

Fiore, A. M., Dentener, F. J., Wild, O., Cuvelier, C., Schultz, M. G., Hess, P., Textor, C., Schulz, M., Doherty, R. M., Horowitz, L. W., MacKenzie, I. A., Sanderson, M. G., Shindell, D. T., Stevenson, D. S., Szopa, S., Van Dingenen, R., Zeng, G., Atherton, C., Bergmann, D., Bey, I., Carmichael, G., Collins, W. J., Duncan, B. N., Faluvegi, G., Folberth, G., Gauss, M., Gong, S., Hauglustaine, D., Holloway, T., Isaksen, I. S. A., Jacob, D. J., Jonson, J. E., Kaminski, J. W., Keating, T. J., Lupu, A., Marmer, E., Montanaro, V., Park, R. J., Pitari, G., Pringle, K. J., Pyle, J. A., Schroeder, S., Vivanco, M. G., Wind, P., Wojcik, G., Wu, S., and Zuber, A.: Multi-model estimates of intercontinental source-receptor relationships for ozone pollution, J. Geophys. Res., 114, D04301, doi:10.1029/2008JD010816, 2009.

Folberth, G. A., Hauglustaine, D. A., Lathière, J., and Brocheton, F.: Interactive chemistry in the Laboratoire de Météorologie Dynamique general circulation model: model description and impact analysis of biogenic hydrocarbons on tropospheric chemistry, Atmos. Chem. Phys., 6, 2273–2319, doi:10.5194/acp-6-2273-2006, 2006.

Forster, P., Ramaswamy, V., Artaxo, P., Berntsen, T., Betts, R., Fahey, D. W., Haywood, J., Lean, J., Lowe, D. C., Myhre, G., Nganga, J., Prinn, R., Raga, G., Schulz, M., and Van Dorland, R.: Changes in atmospheric constituents and in radiative forcing, in: Climate Change 2007: The Physical Science Basis, Contribution of Working Group I to the Fourth Assessment Report of the Intergovernmental Panel on Climate Change, edited by: Solomon, S., Qin, D.,

ACPD
14, 6863–6949, 2014

Manning, M., Chen, Z., Marquis, M., Averyt, K. B., Tignor, M., and Miller, H. L., Cambridge University Press, Cambridge, UK, New York, NY, USA, 2007.
Fouquart, Y. and Bonel, B.: Computations of solar heating of the earth's atmosphere: a new parameterization, Beitr. Phys. Atmos., 53, 35–62, 1980.
Gosse, S. F., Wang, M., Labrie, D., and Chylek, P.: Imaginary part of the refractive index of sulfates and nitrates in the 0.7–2.6 µm spectral region, Appl. Optics, 36, 3622–3634, 1997.
Gruber, N. and Galloway, J. N.: Earth-system perspective of the global nitrogen cycle, Nature, 451, 293–296, 2008.
Hauglustaine, D. A., Hourdin, F., Walters, S., Jourdain, L., Filiberti, M.-A., Larmarque, J.-F., and Holland, E. A.: Interactive chemistry in the Laboratoire de Météorologie Dynamique general circulation model: description and background tropospheric chemistry evaluation, J. Geophys. Res., 109, D04314, doi:10.1029/2003JD003957, 2004.
Heald, C. L., J. L. Collett Jr., Lee, T., Benedict, K. B., Schwandner, F. M., Li, Y., Clarisse, L., Hurtmans, D. R., Van Damme, M., Clerbaux, C., Coheur, P.-F., Philip, S., Martin, R. V., and Pye, H. O. T.: Atmospheric ammonia and particulate inorganic nitrogen over the United States, Atmos. Chem. Phys., 12, 10295–10312, doi:10.5194/acp-12-10295-2012, 2012.
Hertel, O., Reis, S., Skjoth, C. A., Bleeker, A., Harrison, R., Cape, J. N., Fowler, D., Skiba, U., Simpson, D., Jickells, T., Baker, A., Kulmala, M., Gyldenkaerne, S., Sorensen, L. L., and Erisman, J. W.: Nitrogen processes in the atmosphere, in: The European Nitrogen Assessment, edited by: Sutton, M. A., Howard, C. M., Erisman, J. W., Billen, G., Bleeker, A., Grennfelt, P., van Grinsven, H., and Grizzetti, B., Cambridge University Press, Cambridge, 177–207, 2011.
Holben, B. N., Tanre, D., Smirnov, A., Eck, T. F., Slutsker, I., Abuhassan, N., Newcomb, W. W., Schafer, J., Chatenet, B., Lavenue, F., Kaufman, Y. J., Vande Castle, J., Setzer, A., Markham, B., Clark, D., Frouin, R., Halthore, R., Karnieli, A., O'Neill, N. T., Pietras, C., Pinker, R. T., Voss, K., and Zibordi, G.: An emerging ground-based aerosol climatology: aerosol optical depth from AERONET, J. Geophys. Res., 106, 12067–12097, 2001.
Hourdin, F. and Armengaud, A.: The use of finite-volume methods for atmospheric advection of trace species – 1. test of various formulations in a general circulation model, Mon. Weather Rev., 127, 822–837, 1999.
Hourdin, F. and Issartel, J. P.: Sub-surface nuclear tests monitoring through the CTBT xenon network, Geophys. Res. Lett., 27, 2245–2248, 2000.
Hourdin, F., Musat, I., Bony, S., Braconnot, P., Codron, F., Dufresne, J.-L., Fairhead, L., Filiberti, M.-A., Friedlingstein, P., Grandpeix, J.-Y., Krinner, G., Levan, P., Li, Z.-X., and Lott, F.:

ACPD
14, 6863–6949, 2014

The LMDZ4 general circulation model: climate performance and sensitivity to parametrized physics with emphasis on tropical convection, Clim. Dynam., 27, 787–813, 2006.
Hov, O., Eliassen, A., and Simpson, D.: Calculation of the distribution of NO_x compounds in Europe, in: Tropospheric Ozone, Regional and Global Scale Interactions, edited by: Isaksen, I. S. A., 239–261, Reidel, Dordrecht, 1988.
Irshad, R., Grainger, R. G., Peters, D. M., McPheat, R. A., Smith, K. M., and Thomas, G.: Laboratory measurements of the optical properties of sea salt aerosol, Atmos. Chem. Phys., 9, 221–230, doi:10.5194/acp-9-221-2009, 2009.
Jacobson, M. Z.: Studying the effects of calcium and magnesium on size-distributed nitrate and ammonium with EQUISOLV II, Atmos. Environ., 33, 3635–3649, 1999.
Jacobson, M. Z.: Global direct radiative forcing due to multicomponent anthropogenic and natural aerosols, J. Geophys Res., 106, 1551–1568, 2001.
Jarzembski, M. A., Norman, M. L., Fuller, K. A., Srivastava, V., and Cutten, D. R.: Complex refractive index of ammonium nitrate in the 2–20 µm spectral range, Appl. Optics, 42, 922–930, 2003.
Kinne, S., Schulz, M., Textor, C., Guibert, S., Balkanski, Y., Bauer, S. E., Berntsen, T., Berglen, T. F., Boucher, O., Chin, M., Collins, W., Dentener, F., Diehl, T., Easter, R., Feichter, J., Fillmore, D., Ghan, S., Ginoux, P., Gong, S., Grini, A., Hendricks, J., Herzog, M., Horowitz, L., Isaksen, I., Iversen, T., Kirkevåg, A., Kloster, S., Koch, D., Kristjansson, J. E., Krol, M., Lauer, A., Lamarque, J. F., Lesins, G., Liu, X., Lohmann, U., Montanaro, V., Myhre, G., Penner, J., Pitari, G., Reddy, S., Seland, O., Stier, P., Takemura, T., and Tie, X.: An AeroCom initial assessment – optical properties in aerosol component modules of global models, Atmos. Chem. Phys., 6, 1815–1834, doi:10.5194/acp-6-1815-2006, 2006.
Koffi, B., Schulz, M., Breon, F.-M., Griesfeller, J., Winker, D., Balkanski, Y., Bauer, S., Berntsen, T., Chin, M., Collins, W. D., Dentener, F., Diehl, T., Easter, R., Ghan, S., Ginoux, P., Gong, S., Horowitz, L. W., Iversen, T., Kirkevag, A., Koch, D., Krol, M., Myhre, G., Stier, P., and Takemura, T.: Application of the CALIOP layer product to evaluate the vertical distribution of aerosols estimated by global models: AeroCom phase I results, J. Geophys. Res., 117, D10201, doi:10.1029/2011JD016858, 2012.
Krinner, G., Viovy, N., de Noblet-Ducoudre, N., Ogee, J., Polcher, J., Friedlingstein, P., Ciais, P., Sitch, S., and Prentice, I. C.: A dynamic global vegetation model for studies of the coupled atmosphere-biosphere system, Global Biogeochem. Cy., 19, GB1015, doi:10.1029/2003GB002199, 2005.

ACPD
14, 6863–6949, 2014

Lamarque, J.-F., Bond, T. C., Eyring, V., Granier, C., Heil, A., Klimont, Z., Lee, D., Liousse, C., Mieville, A., Owen, B., Schultz, M. G., Shindell, D., Smith, S. J., Stehfest, E., Van Aardenne, J., Cooper, O. R., Kainuma, M., Mahowald, N., McConnell, J. R., Naik, V., Riahi, K., and van Vuuren, D. P.: Historical (1850–2000) gridded anthropogenic and biomass burning emissions of reactive gases and aerosols: methodology and application, Atmos. Chem. Phys., 10, 7017–7039, doi:10.5194/acp-10-7017-2010, 2010.

Lamarque, J.-F., Kyle, G. P., Meinshausen, M., Riahi, K., Smith, S. J., van Vuuren, D. P., Conley, A. J., and Vitt, F.: Global and regional evolution of short-lived radiatively-active gases and aerosols in the Representative Concentration Pathways, Climatic Change, 109, 191–212, doi:10.1007/s10584-011-0155-0, 2011.

Lamarque, J.-F., Dentener, F., McConnell, J., Ro, C.-U., Shaw, M., Vet, R., Bergmann, D., Cameron-Smith, P., Dalsoren, S., Doherty, R., Faluvegi, G., Ghan, S. J., Josse, B., Lee, Y. H., MacKenzie, I. A., Plummer, D., Shindell, D. T., Skeie, R. B., Stevenson, D. S., Strode, S., Zeng, G., Curran, M., Dahl-Jensen, D., Das, S., Fritzsche, D., and Nolan, M.: Multi-model mean nitrogen and sulfur deposition from the Atmospheric Chemistry and Climate Model Intercomparison Project (ACCMIP): evaluation of historical and projected future changes, Atmos. Chem. Phys., 13, 7997–8018, doi:10.5194/acp-13-7997-2013, 2013.

Lathière, J., Hauglustaine, D. A., Friend, A. D., De Noblet-Ducoudré, N., Viovy, N., and Folberth, G. A.: Impact of climate variability and land use changes on global biogenic volatile organic compound emissions, Atmos. Chem. Phys., 6, 2129–2146, doi:10.5194/acp-6-2129-2006, 2006.

Lauer, A., Hendricks, J., Ackermann, I., Schell, B., Hass, H., and Metzger, S.: Simulating aerosol microphysics with the ECHAM/MADE GCM – Part 1: Model description and comparison with observations, Atmos. Chem. Phys., 5, 3251–3276, doi:10.5194/acp-5-3251-2005, 2005.

Li, W. J. and Shao, L. Y.: Observation of nitrate coatings on atmospheric mineral dust particles, Atmos. Chem. Phys., 9, 1863–1871, doi:10.5194/acp-9-1863-2009, 2009.

Liao, H. and Seinfeld, J. H.: Global impacts of gas-phase chemistry-aerosol interactions on direct radiative forcing by anthropogenic aerosols and ozone, J. Geophys. Res., 110, D18208, doi:10.1029/2005JD005907, 2005.

Liao, H., Zhang, Y., Chen, W.-T., Raes, F., and Seinfeld, J. H.: Effect of chemistry-aerosol-climate coupling on predictions of future climate and future levels of tropospheric ozone and aerosols, J. Geophys. Res., 114, D10306, doi:10.1029/2008JD010984, 2009.

ACPD
14, 6863–6949, 2014

Martin, S. T., Schlenker, J. C., Malinowski, A., Hung, H.-M., and Rudich, Y.: Crystallization of atmospheric sulfate-nitrate-ammonium particles, Geophys. Res. Lett., 30, 2102, doi:10.1029/2003GL017930, 2003.

Martin, S. T., Hung, H.-M., Park, R. J., Jacob, D. J., Spurr, R. J. D., Chance, K. V., and Chin, M.: Effects of the physical state of tropospheric ammonium-sulfate-nitrate particles on global aerosol direct radiative forcing, Atmos. Chem. Phys., 4, 183–214, doi:10.5194/acp-4-183-2004, 2004.

Metzger, S., Dentener, F., Pandis, S., and Lelieveld, J.: Gas/aerosol partitioning: 1. A computationally efficient model, J. Geophys. Res., 107, 4312, doi:10.1029/2001JD001102, 2002a.

Metzger, S., Dentener, F., Krol, M., Jeuken, A., and Lelieveld, J.: Gas/aerosol partitioning: 2. Global modeling results, J. Geophys. Res., 107, 4312, doi:10.1029/2001JD001103, 2002b.

Mozurkewich, M.: The dissociation constant of ammonium nitrate and its dependence on temperature, relative humidity and particle size, Atmos. Environ. A-Gen., 27, 261–270, 1993.

Myhre, G., Grini, A., and Metzger, S.: Modelling of nitrate and ammonium-containing aerosols in presence of sea salt, Atmos. Chem. Phys., 6, 4809–4821, doi:10.5194/acp-6-4809-2006, 2006.

Myhre, G., Samset, B. H., Schulz, M., Balkanski, Y., Bauer, S., Berntsen, T. K., Bian, H., Bellouin, N., Chin, M., Diehl, T., Easter, R. C., Feichter, J., Ghan, S. J., Hauglustaine, D., Iversen, T., Kinne, S., Kirkevåg, A., Lamarque, J.-F., Lin, G., Liu, X., Lund, M. T., Luo, G., Ma, X., van Noije, T., Penner, J. E., Rasch, P. J., Ruiz, A., Seland, Ø., Skeie, R. B., Stier, P., Takemura, T., Tsigaridis, K., Wang, P., Wang, Z., Xu, L., Yu, H., Yu, F., Yoon, J.-H., Zhang, K., Zhang, H., and Zhou, C.: Radiative forcing of the direct aerosol effect from AeroCom Phase II simulations, Atmos. Chem. Phys., 13, 1853–1877, doi:10.5194/acp-13-1853-2013, 2013.

Olivier, J. G. J., Bouwman, A. F., Van der Hoek, K. W., and Berdowski, J. J. M.: Global air emission inventories for anthropogenic sources of NO_x, NH_3, and N_2O in 1990, Environ. Pollut., 102, 135–148, 1998.

Park, R. J., Jacob, D. J., Field, B. D., Yantosca, R. M., and Chian, M.: Natural and transboundary pollution influences on sulfate-nitrate-ammonium aerosols in the United States: implications for policy, J. Geophys. Res., 109, D15204, doi:10.1029/2003JD004473, 2004.

Pilinis, C. and Seinfeld, J. H.: Continued development of a general equilibrium model for inorganic multicomponent atmospheric aerosols, Atmos. Environ., 21, 2453–2466, 1987.

Pilinis, C., Capaldo, K. P., Nenes, A., and Pandis, S. N.: MADM – a new multicomponent aerosol dynamics model, Aerosol Sci. Tech., 32, 482–502, 2000.

ACPD
14, 6863–6949, 2014

Pringle, K. J., Tost, H., Message, S., Steil, B., Giannadaki, D., Nenes, A., Fountoukis, C., Stier, P., Vignati, E., and Lelieveld, J.: Description and evaluation of GMXe: a new aerosol submodel for global simulations (v1), Geosci. Model Dev., 3, 391–412, doi:10.5194/gmd-3-391-2010, 2010.

Putaud, J.-P., Raes, F., Van Dingenen, R., Brüggemann, E., Facchini, M.-C., Decesari, S., Fuzzi, S., Gehrig, R., Hüglin, C., Laj, P., Lorbeer, G., Maenhaut, W., Mihalopoulos, N., Müller, K., Querol, X., Rodriguez, S., Schneider, J., Spindler, G., ten Brink, H., Tørseth, K., and Wiedensohler, A.: European aerosol phenomenology-2: chemical characteristics of particulate matter at kerbside, urban, rural and background sites in Europe, Atmos. Environ., 38, 2579–2595, 2004a.

Putaud, J.-P., Van Dingenen, R., Dell'Acqua, A., Raes, F., Matta, E., Decesari, S., Facchini, M. C., and Fuzzi, S.: Size-segregated aerosol mass closure and chemical composition in Monte Cimone (I) during MINATROC, Atmos. Chem. Phys., 4, 889–902, doi:10.5194/acp-4-889-2004, 2004.

Reidmiller, D. R., Fiore, A. M., Jaffe, D. A., Bergmann, D., Cuvelier, C., Dentener, F. J., Duncan, B. N., Folberth, G., Gauss, M., Gong, S., Hess, P., Jonson, J. E., Keating, T., Lupu, A., Marmer, E., Park, R., Schultz, M. G., Shindell, D. T., Szopa, S., Vivanco, M. G., Wild, O., and Zuber, A.: The influence of foreign vs. North American emissions on surface ozone in the US, Atmos. Chem. Phys., 9, 5027–5042, doi:10.5194/acp-9-5027-2009, 2009.

Sander, S. P., Abbatt, J., Barker, J. R., Burkholder, J. B., Friedl, R. R., Golden, D. M., Huie, R. E., Kolb, C. E., Kurylo, M. J., Moortgat, G. K., Orkin, V. L., and Wine, P. H.: Chemical Kinetics and Photochemical Data for Use in Atmospheric Studies, Evaluation No. 17, JPL Publication 10-6, Jet Propulsion Laboratory, Pasadena, 2011.

Schaap, M., van Loon, M., ten Brink, H. M., Dentener, F. J., and Builtjes, P. J. H.: Secondary inorganic aerosol simulations for Europe with special attention to nitrate, Atmos. Chem. Phys., 4, 857–874, doi:10.5194/acp-4-857-2004, 2004.

Schulz, M.: Constraining Model Estimates of the Aerosol Radiative Forcing, Thèse d'Habilitation à Diriger des Recherches, Université Pierre et Marie Curie, Paris VI, 2007.

Schulz, M., Balkanski, Y., Dulac, F., and Guelle, W.: Role of aerosol size distribution and source location in a three-dimensional simulation of a Saharan dust episode tested against satellite-derived optical thickness, J. Geophys. Res., 103, 10579–10592, 1998.

Schulz, M., Textor, C., Kinne, S., Balkanski, Y., Bauer, S., Berntsen, T., Berglen, T., Boucher, O., Dentener, F., Guibert, S., Isaksen, I. S. A., Iversen, T., Koch, D., Kirkevåg, A., Liu, X., Monta-

ACPD
14, 6863–6949, 2014

naro, V., Myhre, G., Penner, J. E., Pitari, G., Reddy, S., Seland, Ø., Stier, P., and Takemura, T.: Radiative forcing by aerosols as derived from the AeroCom present-day and pre-industrial simulations, Atmos. Chem. Phys., 6, 5225–5246, doi:10.5194/acp-6-5225-2006, 2006.

Schulz, M., Gauss, M., Benedictow, A., Jonson, J. E., Tsyro, S., Nyiri, A., Simpson, D., Steensen, B. M., Klein, H., Valdebenito, A., Wind, P., Kirkevåg, A., Griesfeller, J., Bartnicki, J., Olivié, D., Grini, A., Iversen, T., Seland, Ø., Semeena, V. S., Fagerli, H., Aas, W., Hjellbrekke, A.-G., Mareckova, K., Wankmuller, R., Schneider, P., Solberg, S., Svendby, T., Liu, L., Posch, M., Vieno, M., Reis, S., Kryza, M., Werner, M., and Walaszek, K.: Transboundary acidification, euthropication and ground level ozone in Europe in 2011, EMEP Report 1/2013, Norwegian Meteorological Institute, ISSN 1504–6109, Oslo, Norway, 2013.

Schwartz, S. E.: Mass transport considerations pertinent to aqueous-phase reactions of gases in liquid-water clouds, in: Chemistry of Multiphase Atmospheric Systems, edited by: Jaeschke, W., Springer, New York, 415–471, 1986.

Seinfeld, J. H. and Pandis, S. N.: Atmospheric Chemistry and Physics, John Wiley and Sons, New York, 1998.

Shindell, D. T., Lamarque, J.-F., Schulz, M., Flanner, M., Jiao, C., Chin, M., Young, P. J., Lee, Y. H., Rotstayn, L., Mahowald, N., Milly, G., Faluvegi, G., Balkanski, Y., Collins, W. J., Conley, A. J., Dalsoren, S., Easter, R., Ghan, S., Horowitz, L., Liu, X., Myhre, G., Nagashima, T., Naik, V., Rumbold, S. T., Skeie, R., Sudo, K., Szopa, S., Takemura, T., Voulgarakis, A., Yoon, J.-H., and Lo, F.: Radiative forcing in the ACCMIP historical and future climate simulations, Atmos. Chem. Phys., 13, 2939–2974, doi:10.5194/acp-13-2939-2013, 2013.

Sun, Q. and Wexler, A. S.: Modeling urban and regional aerosols near acid neutrality application to the 24–25 June SCAQS episode, Atmos. Environ., 32, 3533–3545, 1998.

Sutton, M. A., Dragosits, U., Tang, Y. S., and Fowler, D.: Ammonia emissions from non-agricultural sources in the UK, Atmos. Environ., 34, 855–869, 2000.

Szopa, S., Balkanski, Y., Schulz, M., Bekki, S., Cugnet, D., Fortems-Cheiney, A., Turquety, S., Cozic, A., Deandreis, C., Hauglustaine, D., Idelkadi, A., Lathiere, J., Marchand, M., Yan, N., and Dufresne, J.-L.: Aerosol and ozone changes as forcing for climate evolution between 1850 and 2100, Clim. Dynam., 40, 2223–2250, doi:10.1007/s00382-012-1408-y, 2012.

Tang, I. N.: Chemical and size effects of hygroscopic aerosols on light scattering coefficients, J. Geophys. Res., 101, 2156–2202, doi:10.1029/96JD03003, 1996.

ACPD
14, 6863–6949, 2014

Tie, X., Madronich, S., Walters, S., Edwards, D. P., Ginoux, P., Mahowald, N., Zhang, R. Y., Lou, C., and Brasseur, G.: Assessment of the global impact of aerosols on tropospheric oxidants, J. Geophys. Res., 110, D03204, doi:10.1029/2004JD005359, 2005.

van Dorland, R., Dentener, F. J., and Lelieveld, J.: Radiative forcing due to tropospheric ozone and sulphate aerosols, J. Geophys. Res., 102, 28079–28100, 1997.

Van Leer, B.: Towards the ultimate conservative difference scheme – Part 4: a new approach to numerical convection, J. Comput. Phys., 23, 276–299, 1977.

Wang, R., Tao, S., Wang, W., Liu, J., Shen, H., Shen, G., Wang, B., Liu, X., Li, W., Huang, Y., Zhang, Y., Lu, Y., Chen, H., Chen, Y., Wang, C., Zhu, D., Wang, X., Li, B., Liu, W., and Ma., J.: Black carbon emissions in China from 1949 to 2050, Environ. Sci. Technol., 46, 7595–7603, 2012.

Xu, L. and Penner, J. E.: Global simulations of nitrate and ammonium aerosols and their radiative effects, Atmos. Chem. Phys., 12, 9479–9504, doi:10.5194/acp-12-9479-2012, 2012.

Zhang, L., Jacob, D. J., Knipping, E. M., Kumar, N., Munger, J. W., Carouge, C. C., van Donkelaar, A., Wang, Y. X., and Chen, D.: Nitrogen deposition to the United States: distribution, sources, and processes, Atmos. Chem. Phys., 12, 4539–4554, doi:10.5194/acp-12-4539-2012, 2012.

Zhang, Y., Seigneur, C., Seinfeld, J. H., Jacobson, M., Clegg, S. L., and Binkowski, F. S.: A comparative review of inorganic aerosol thermodynamic equilibrium modules: similarities, differences, and their likely causes, Atmos. Environ., 34, 117–137, 2000.

ACPD
14, 6863–6949, 2014

Table 1. Total (anthropogenic + natural) and global emissions of NO_x and NH_3 ($TgN\,yr^{-1}$), SO_2 ($TgS\,yr^{-1}$), Black Carbon (BC) and Organic Carbon (OC) ($Tg\,yr^{-1}$) for the various simulations performed in this study.

Scenario	NO_x	NH_3	SO_2	BC	OC
1850	10	21	10	3	22
2000	46	50	59	8	36
2030 RCP2.6	39	62	35	7	36
2050 RCP2.6	36	67	22	5	30
2100 RCP2.6	24	79	14	3	25
2030 RCP4.5	42	56	49	7	29
2050 RCP4.5	36	57	32	6	27
2100 RCP4.5	24	54	18	4	19
2030 RCP6.0	40	57	45	7	36
2050 RCP6.0	37	64	43	7	36
2100 RCP6.0	23	72	17	4	32
2030 RCP8.5	48	63	48	7	33
2050 RCP8.5	40	69	32	6	30
2100 RCP8.5	31	78	20	4	24
Sensitivity simulations					
2100 RCP4.5-NO_x	31	54	18	4	19
2100 RCP4.5-NH_3	24	78	18	4	19
2100 RCP4.5-SO_2	24	54	59	4	19

ACPD
14, 6863–6949, 2014

Table 2. Tropospheric budget of nitric acid (HNO_3) and nitrate particles (NO_3^-) for the "pre-industrial" (1850) and "present-day" (2000) simulations. The budget terms for HNO_3 are integrated up to 200 hPa.

	1850	2000
HNO_3		
Sources ($Tg\,N\,yr^{-1}$)	14.09	48.51
Gas phase	14.04	44.59
Aerosols	0.05	3.92
Loss ($Tg\,N\,yr^{-1}$)	14.80	49.46
Gas phase	1.55	3.42
Fine nitrates	0.28	3.19
Dust nitrates	2.96	6.26
Sea-salt nitrates	1.57	4.92
Dry deposition	3.42	14.66
Wet deposition	5.02	17.02
Burden ($Tg\,N$)	0.14	0.30
Lifetime (days)	3.57	2.25
NO_3^-		
Sources ($Tg\,N\,yr^{-1}$)	4.81	14.37
Fine	0.28	3.19
Dust	2.96	6.26
Sea-salt	1.57	4.92
Loss ($Tg\,N\,yr^{-1}$)	4.80	14.33
Dry deposition	0.32	1.66
Wet deposition	4.49	12.67
Burden ($Tg\,N$)	0.09	0.18
Fine	0.01	0.05
Dust	0.04	0.07
Sea-salt	0.03	0.06
Lifetime (days)	6.75	4.61

ACPD
14, 6863–6949, 2014

Table 3. Troposheric budget of ammonia (NH_3) and ammonium particles (NH_4^+) for the "pre-industrial" (1850) and "present-day" (2000) simulations.

	1850	2000
NH_3		
Sources: emissions ($Tg\,N\,yr^{-1}$)	20.99	50.51
Loss ($Tg\,N\,yr^{-1}$)	20.98	50.47
Gas phase	0.28	0.63
Ammonium formation	5.14	17.46
Dry deposition	9.67	21.33
Wet deposition	5.89	11.05
Burden ($Tg\,N$)	0.05	0.09
Lifetime (days)	0.81	0.63
NH_4^+		
Sources: ammonia conversion ($Tg\,N\,yr^{-1}$)	5.14	17.46
Loss ($Tg\,N\,yr^{-1}$)	5.13	17.42
Dry deposition	0.32	2.50
Wet deposition	4.81	14.91
Burden ($Tg\,N$)	0.08	0.22
Lifetime (days)	5.39	4.52

ACPD
14, 6863–6949, 2014

Table 4. Evolution of the tropospheric burdens of gaseous and particulate species for the various simulations performed in this study. Units: Tg N, except SO_4^{2-} (Tg S).

Scenario	HNO_3	NH_3	NH_4^+	SO_4^{2-}	Fine NO_3^-	Coarse NO_3^-
1850	0.14	0.05	0.08	0.19	0.01	0.08
2000	0.30	0.09	0.21	0.42	0.05	0.13
2030 RCP2.6	0.25	0.14	0.23	0.33	0.09	0.12
2050 RCP2.6	0.24	0.17	0.22	0.27	0.11	0.12
2100 RCP2.6	0.16	0.26	0.21	0.22	0.12	0.09
2030 RCP4.5	0.28	0.11	0.23	0.39	0.07	0.13
2050 RCP4.5	0.26	0.13	0.21	0.31	0.08	0.12
2100 RCP4.5	0.24	0.14	0.17	0.24	0.07	0.11
2030 RCP6.0	0.28	0.11	0.22	0.37	0.07	0.12
2050 RCP6.0	0.27	0.14	0.24	0.36	0.09	0.12
2100 RCP6.0	0.19	0.21	0.21	0.24	0.11	0.10
2030 RCP8.5	0.32	0.12	0.25	0.39	0.09	0.14
2050 RCP8.5	0.28	0.16	0.24	0.32	0.11	0.13
2100 RCP8.5	0.27	0.23	0.24	0.25	0.13	0.12
Sensitivity simulations						
2100 RCP4.5-NO_x	0.27	0.14	0.18	0.24	0.08	0.12
2100 RCP4.5-NH_3	0.21	0.24	0.22	0.24	0.12	0.10
2100 RCP4.5-SO_2	0.26	0.12	0.21	0.42	0.05	0.11

ACPD
14, 6863–6949, 2014

Table 5. Aerosol Optical Depth (AOD) at 550 nm (X 1000) for 1850 and 2000 and anthropogenic AOD (X 1000) for the various simulations performed in this study. The anthropogenic AOD is calculated by substracting the 1850 AOD to the considered scenario.

Scenario	NO_3^-	SO_4^{2-}	OC	BC	Total
Aerosol Optical Depth					
1850	1.70	14.70	13.67	1.14	31.18
2000	5.27	32.18	18.77	2.45	58.67
Anthropogenic Aerosol Optical Depth					
2000	3.57	17.51	5.09	1.31	27.49
2030 RCP2.6	7.41	9.92	5.42	1.49	24.23
2050 RCP2.6	8.19	5.15	3.55	0.87	17.76
2100 RCP2.6	8.02	2.03	2.10	0.35	12.49
2030 RCP4.5	5.55	14.59	2.93	1.51	24.58
2050 RCP4.5	6.20	8.42	2.52	1.23	18.38
2100 RCP4.5	5.26	3.36	0.31	0.43	9.36
2030 RCP6.0	5.77	13.08	4.96	1.53	25.35
2050 RCP6.0	7.00	12.40	5.34	1.46	26.20
2100 RCP6.0	7.57	3.15	4.84	0.79	16.35
2030 RCP8.5	7.39	14.57	4.48	1.46	27.89
2050 RCP8.5	8.63	8.94	3.31	1.11	21.99
2100 RCP8.5	9.57	4.20	1.75	0.66	16.17

ACPD
14, 6863–6949, 2014

Table 6. All-sky direct radiative forcing at the Top of the Atmosphere (TOA) of the various aerosol components since the 1850 period and future evolution under the different scenarios considered in this study ($mW\,m^{-2}$).

Scenario	NO_3^-	SO_4^{2-}	OC	BC	Total
2000	−56	−315	−56	194	−234
2030 RCP2.6	−95	−118	−60	182	−153
2050 RCP2.6	−102	−94	−39	107	−130
2100 RCP2.6	−96	−33	−25	40	−113
2030 RCP4.5	−76	−270	−29	187	−189
2050 RCP4.5	−78	−159	−25	152	−110
2100 RCP4.5	−60	−60	−3	53	−70
2030 RCP6.0	−79	−235	−57	187	−184
2050 RCP6.0	−94	−225	−59	180	−198
2100 RCP6.0	−91	−58	−55	98	−106
2030 RCP8.5	−101	−273	−49	181	−241
2050 RCP8.5	−108	−173	−40	138	−184
2100 RCP8.5	−115	−79	−18	82	−130

ACPD
14, 6863–6949, 2014

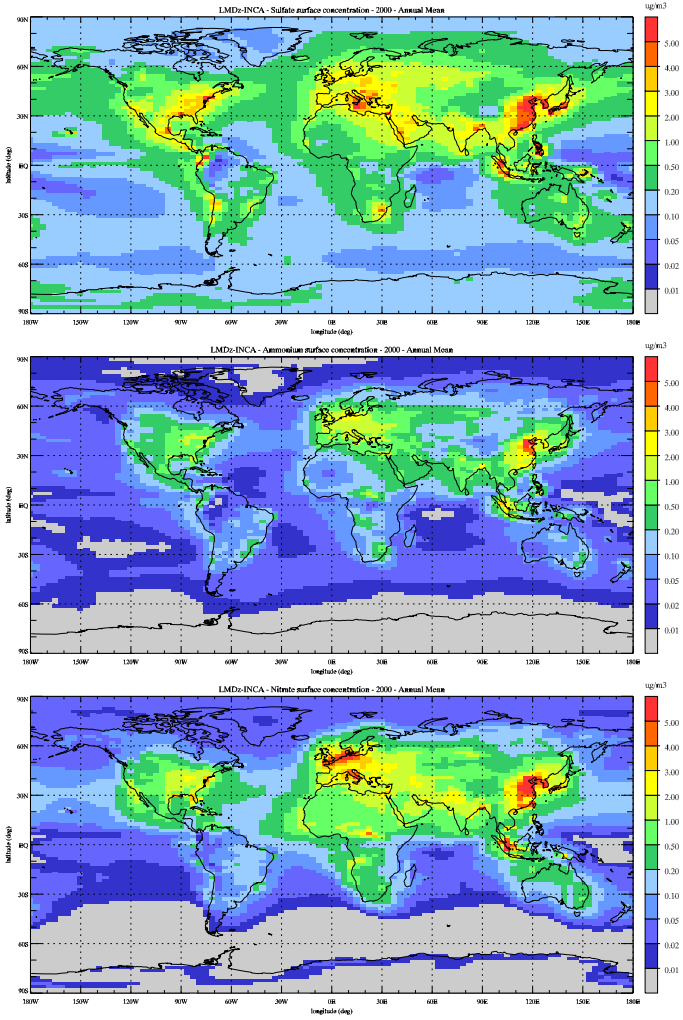

ACPD
14, 6863–6949, 2014

A global model simulation of present and future nitrate aerosols

D. A. Hauglustaine et al.

Fig. 1. Annual mean surface concentration of (top) sulfate aerosols, (middle) ammonium aerosols, and (bottom) total nitrate aerosols simulated for present-day conditions ($\mu g\,m^{-3}$).

ACPD
14, 6863–6949, 2014

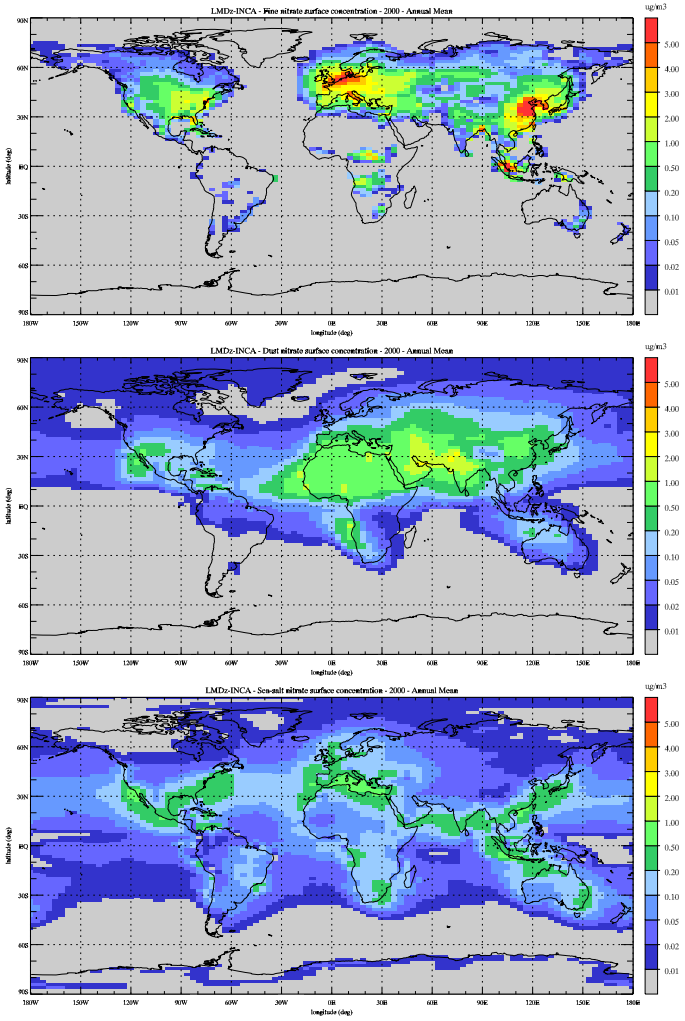

ACPD
14, 6863–6949, 2014

A global model simulation of present and future nitrate aerosols

D. A. Hauglustaine et al.

Fig. 2. Annual mean surface concentration of (top) fine mode nitrate aerosols, (middle) coarse mode nitrates on dust, and (bottom) coarse mode nitrates on sea-salt simulated for present-day conditions ($\mu g\,m^{-3}$).

ACPD
14, 6863–6949, 2014

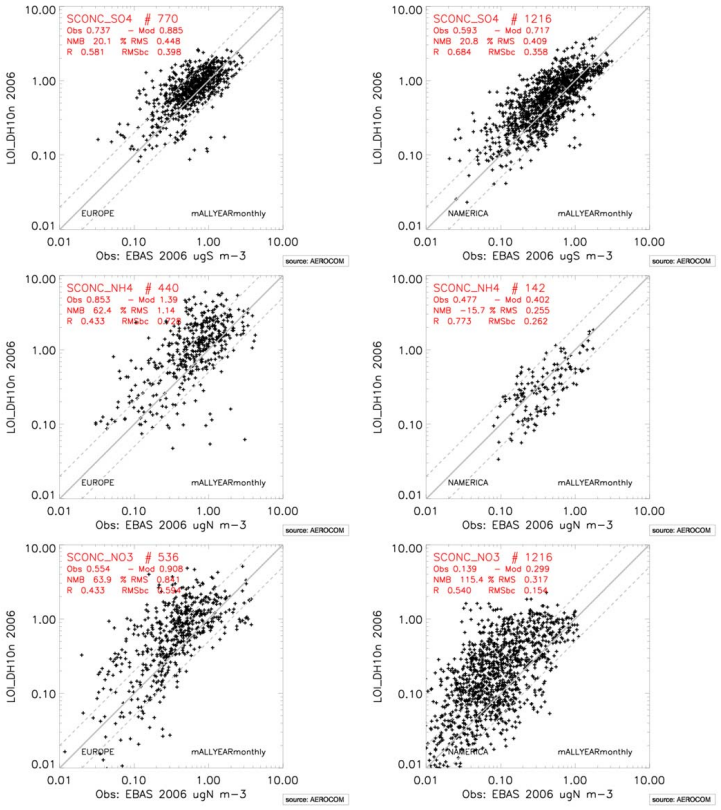

Fig. 3. Simulated surface concentration of sulfates ($\mu S m^{-3}$), ammonium ($\mu N m^{-3}$), and nitrates ($\mu N m^{-3}$) for the year 2006 compared to EBAS data over Europe (left) and Northern America (right). Dashed lines indicate 1 : 2 and 2 : 1 ratios.

ACPD
14, 6863–6949, 2014

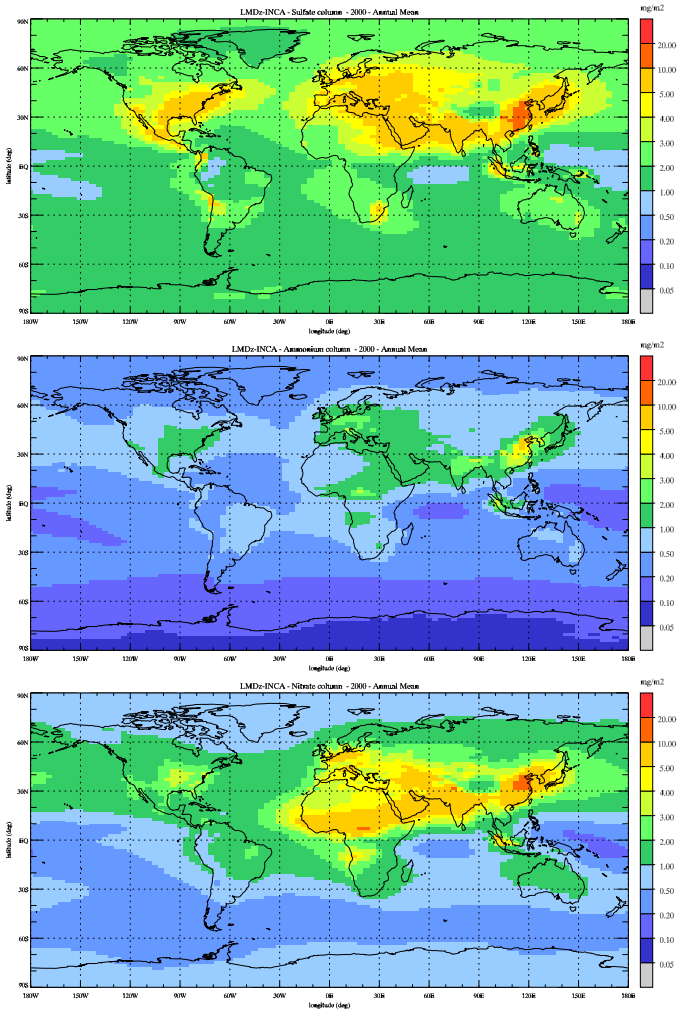

ACPD
14, 6863–6949, 2014

A global model simulation of present and future nitrate aerosols

D. A. Hauglustaine et al.

Fig. 4. Annual mean tropospheric column of (top) sulfate aerosols, (middle) ammonium aerosols, and (bottom) total nitrate aerosols simulated for present-day conditions ($mg\,m^{-2}$).

ACPD
14, 6863–6949, 2014

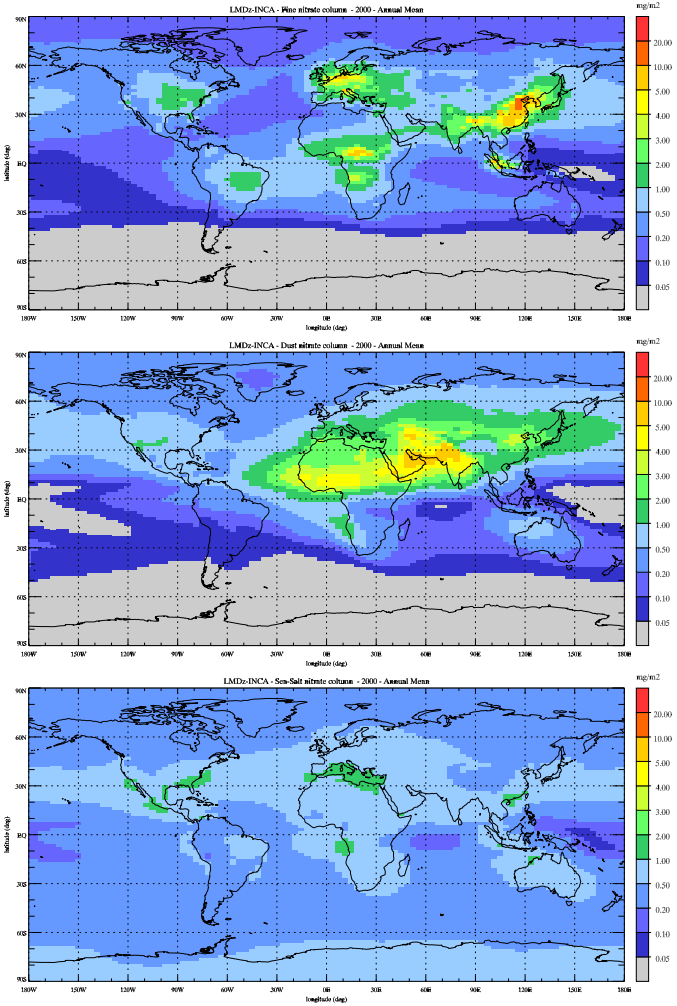

ACPD
14, 6863–6949, 2014

A global model simulation of present and future nitrate aerosols

D. A. Hauglustaine et al.

Fig. 5. Annual mean tropospheric column of (top) fine mode nitrate aerosols, (middle) coarse mode nitrates on dust, and (bottom) coarse mode nitrates on sea-salt simulated for present-day conditions ($mg\,m^{-2}$).

ACPD
14, 6863–6949, 2014

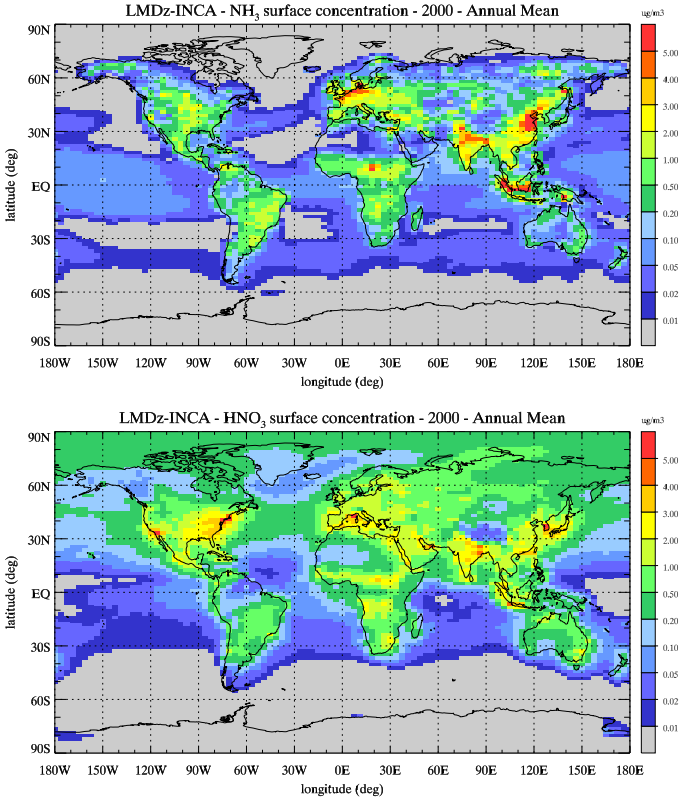

Fig. 6. Annual mean surface concentration of (top) ammonia, and (bottom) nitric acid simulated for present-day conditions ($\mu g\,m^{-3}$).

ACPD
14, 6863–6949, 2014

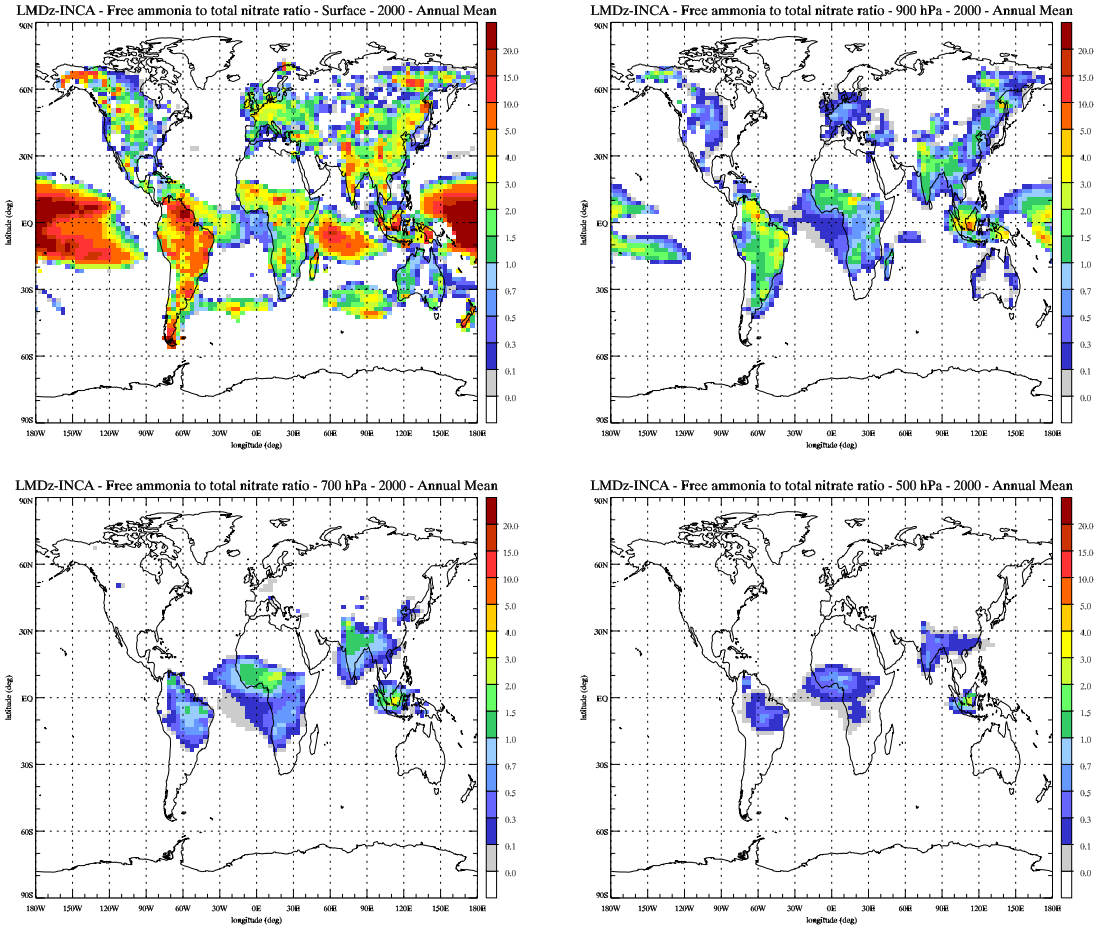

Fig. 7. Annual mean free ammonia to total nitrate ratio calculated for present-day conditions at the surface, 900 hPa, 700 hPa, and 500 hPa.

ACPD
14, 6863–6949, 2014

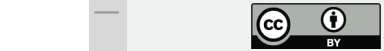

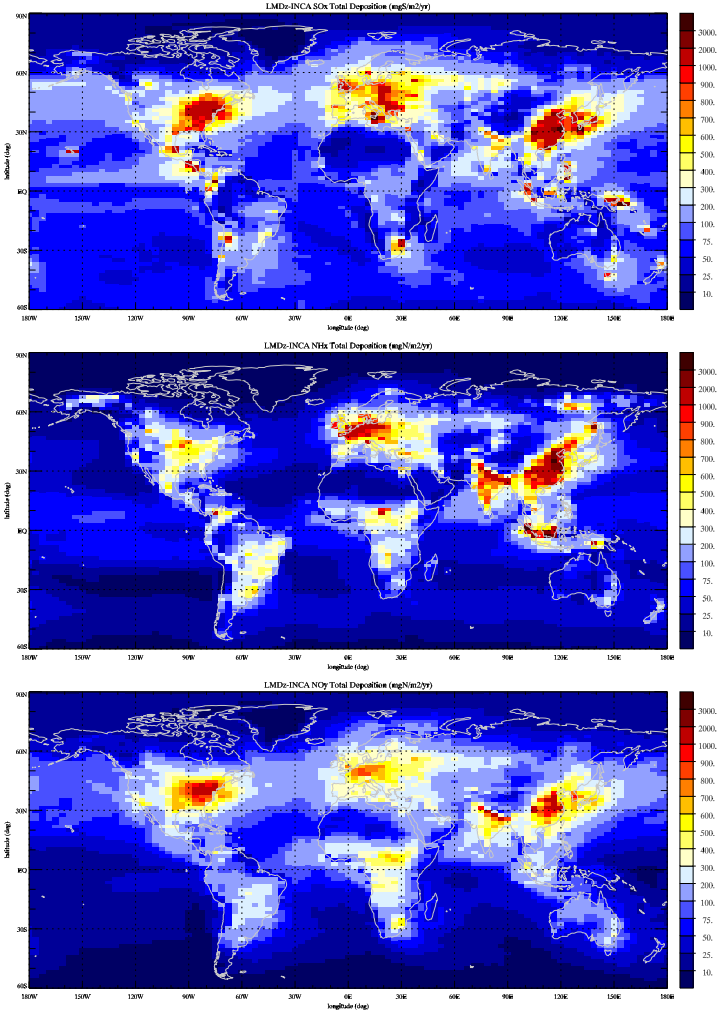

ACPD
14, 6863–6949, 2014

A global model simulation of present and future nitrate aerosols

D. A. Hauglustaine et al.

Fig. 8. Annual mean SO_x ($mg\,S\,m^{-2}\,yr^{-1}$), NH_x, and NO_y ($mg\,N\,m^{-2}\,yr^{-1}$) total surface deposition calculated for present-day conditions.

ACPD
14, 6863–6949, 2014

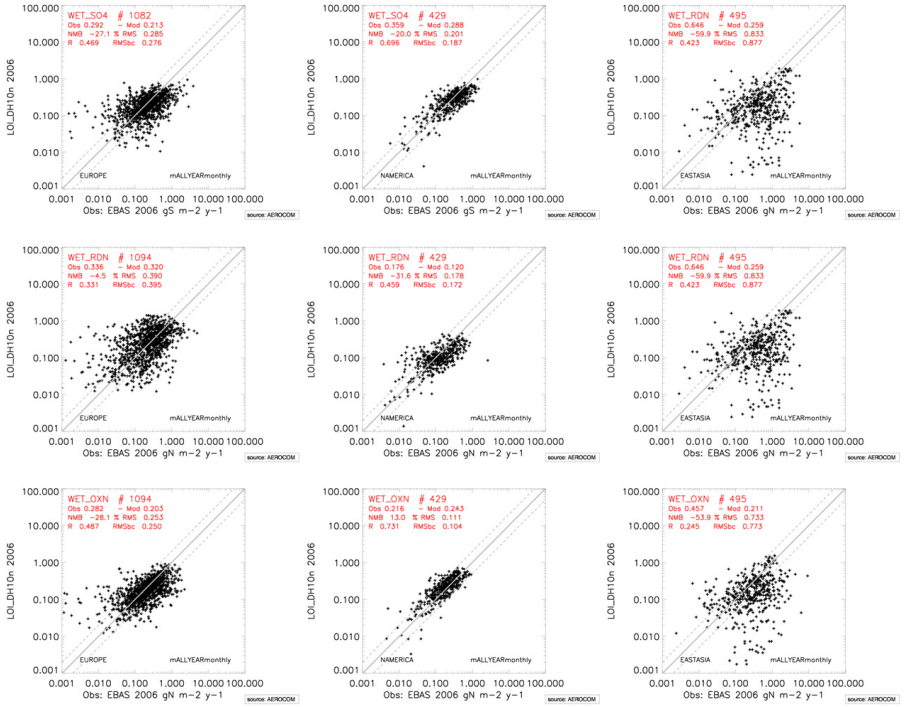

Fig. 9. Simulated SO_x ($gS\,m^{-2}\,yr^{-1}$), NH_x and NO_y ($gN\,m^{-2}\,yr^{-1}$) wet deposition for the year 2006 compared to EBAS data over Europe (left), Northern America (middle), and Eastern Asia (right). Dashed lines indicate 1 : 2 and 2 : 1 ratios.

ACPD
14, 6863–6949, 2014

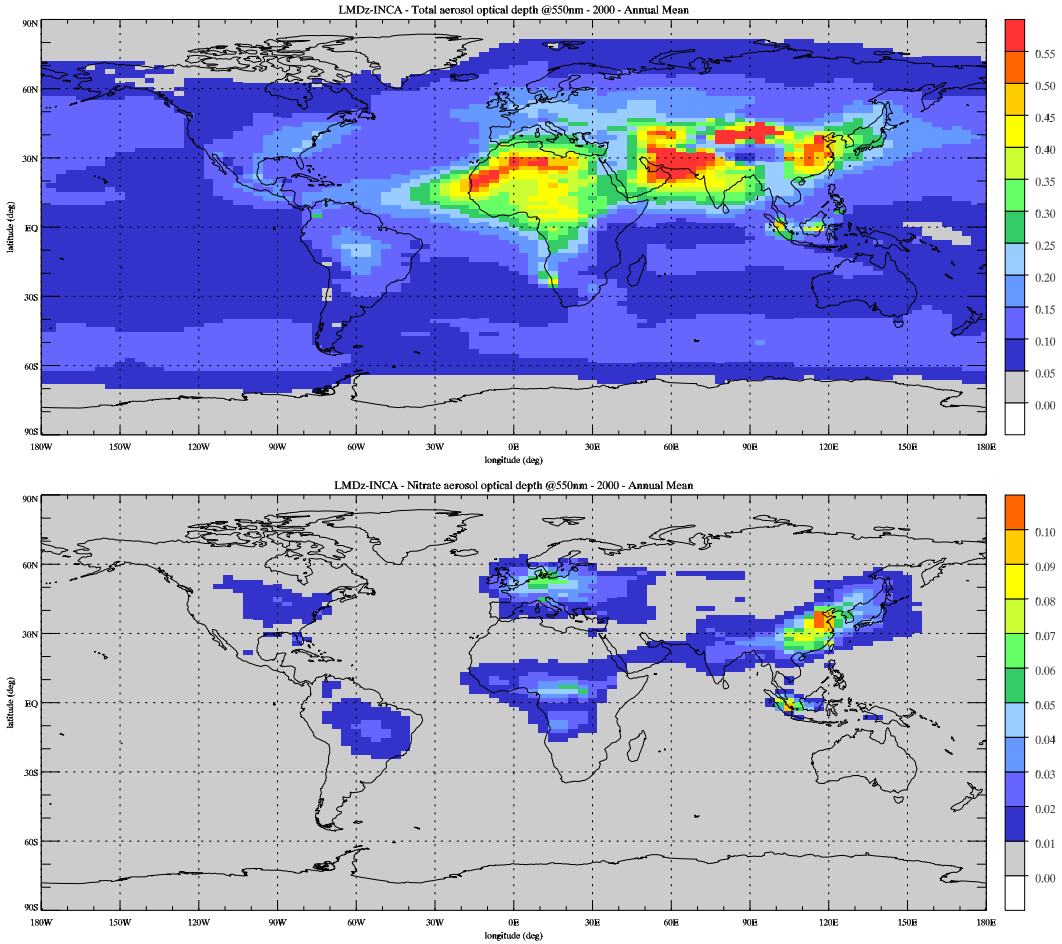

Fig. 10. Annual mean total aerosol optical depth at 550 nm (top), and nitrate aerosol optical depth (bottom) simulated for present-day conditions.

ACPD
14, 6863–6949, 2014

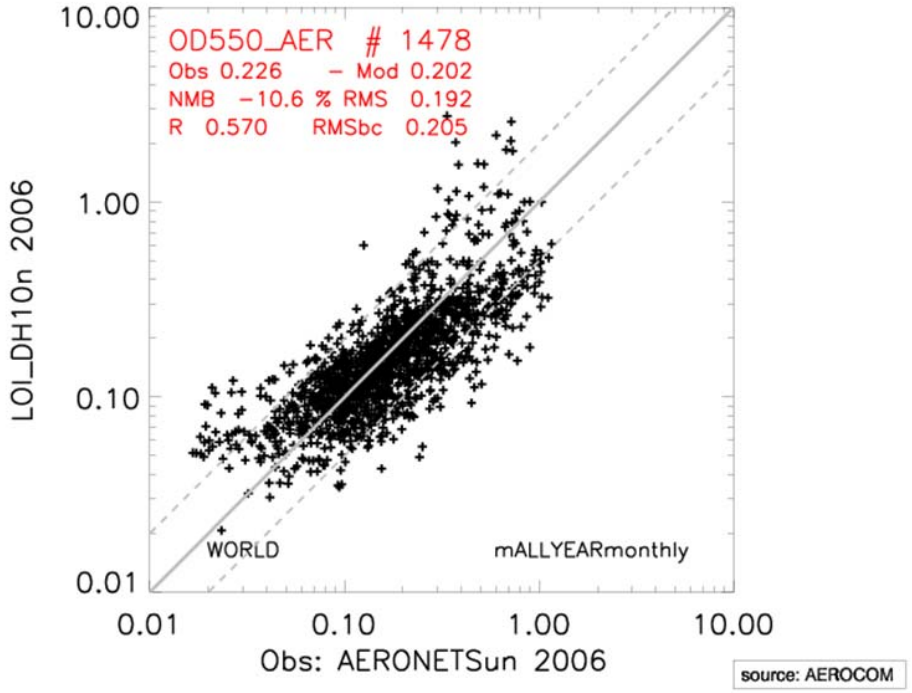

Fig. 11. Simulated total aerosol optical depth at 550 nm for the year 2006 compared to the AERONET data worldwide. Dashed lines indicate 1 : 2 and 2 : 1 ratios.

ACPD
14, 6863–6949, 2014

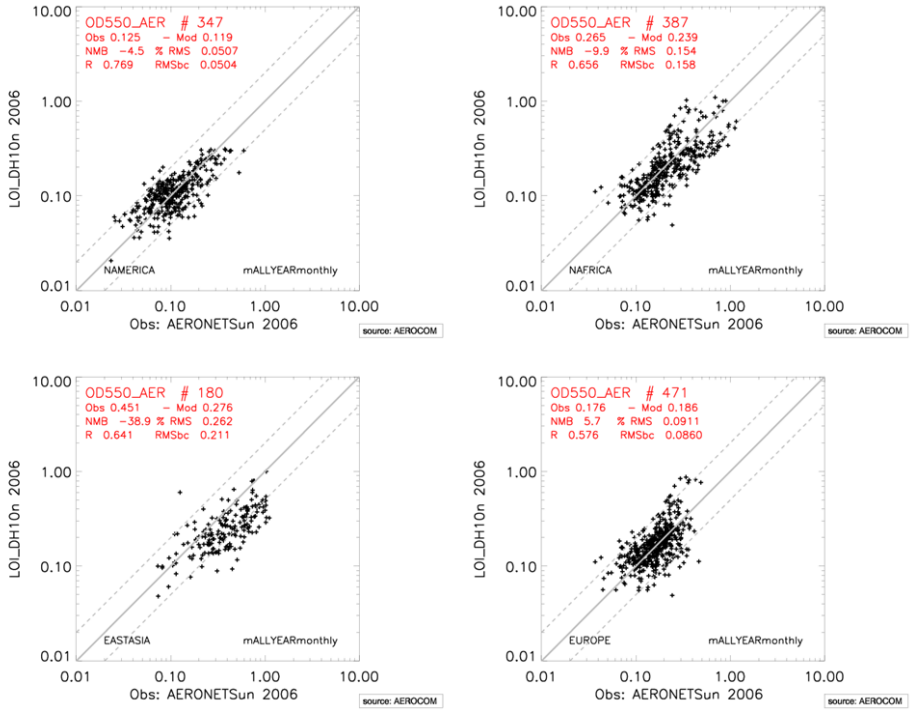

Fig. 12. Simulated total aerosol optical depth at 550 nm for the year 2006 compared to AERONET data for Northern America, Northern Africa, Eastern Asia, and Europe. Dashed lines indicate 1 : 2 and 2 : 1 ratios.

ACPD
14, 6863–6949, 2014

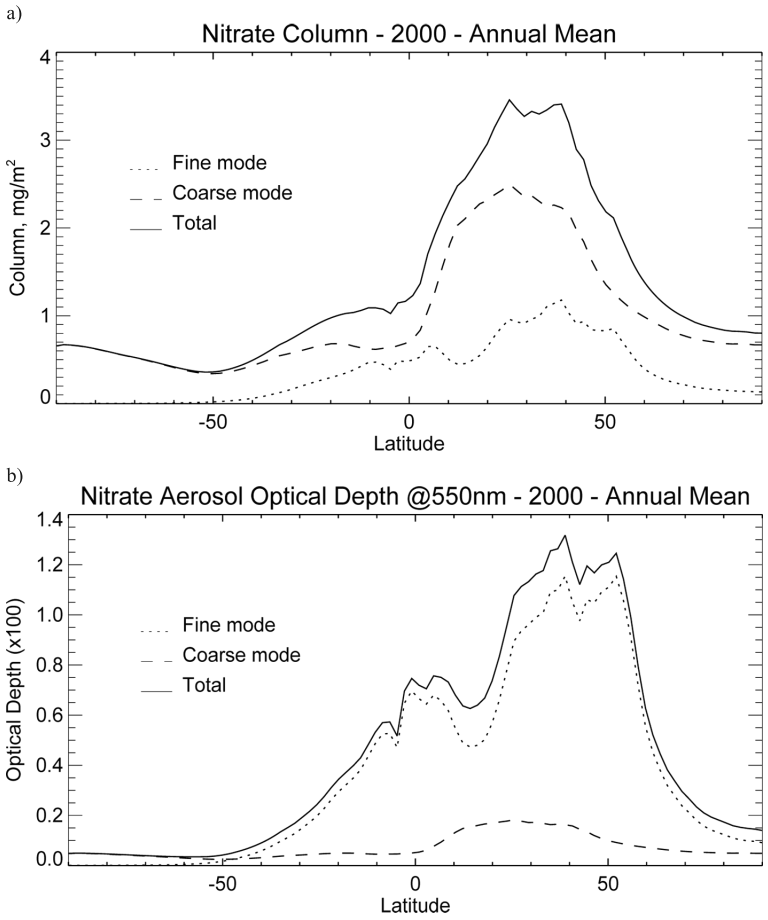

Fig. 13. (a) zonal and annual mean total (solid line), coarse mode (dashed line) and fine mode (dotted line) nitrate particles column ($mg\,m^{-2}$); **(b)** corresponding total, coarse, and fine nitrate particles optical depth at 550 nm (×100).

ACPD
14, 6863–6949, 2014

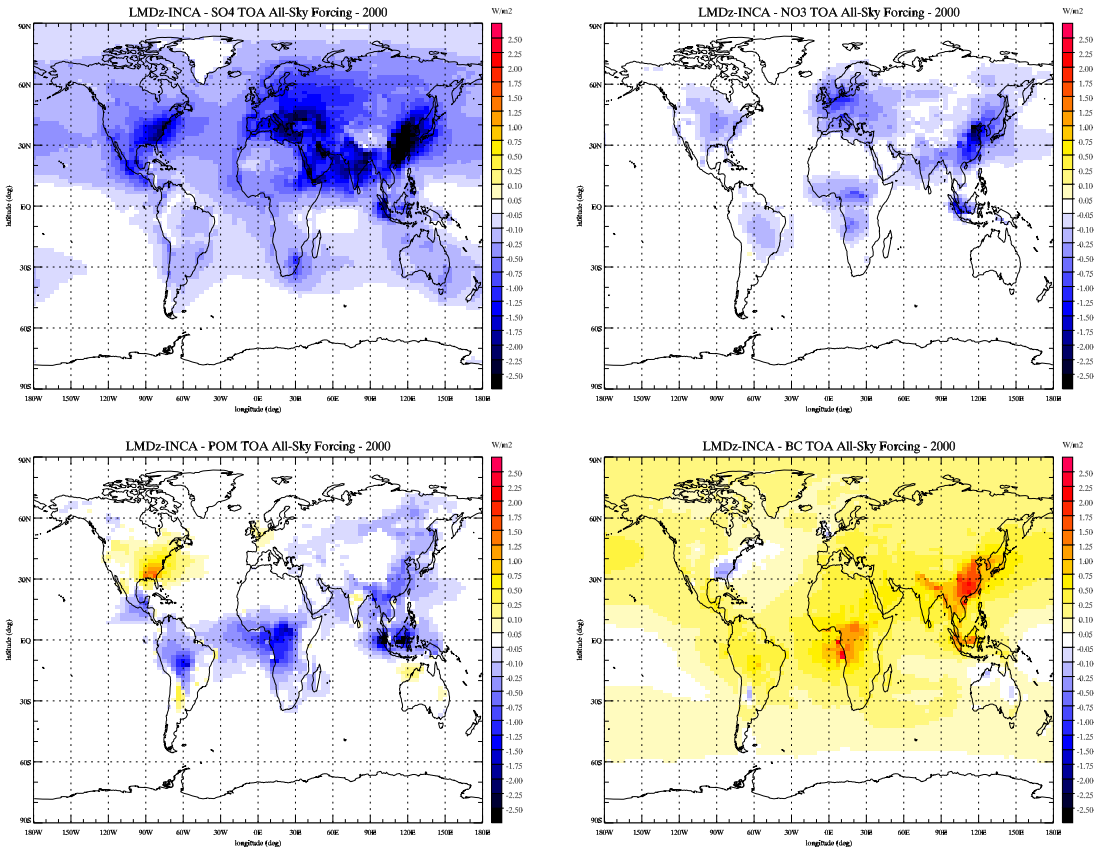

Fig. 14. All-sky top of the atmosphere direct radiative forcing of sulfates, nitrates, organic carbon, and black carbon particles ($W m^{-2}$) calculated for present-day conditions.

ACPD
14, 6863–6949, 2014

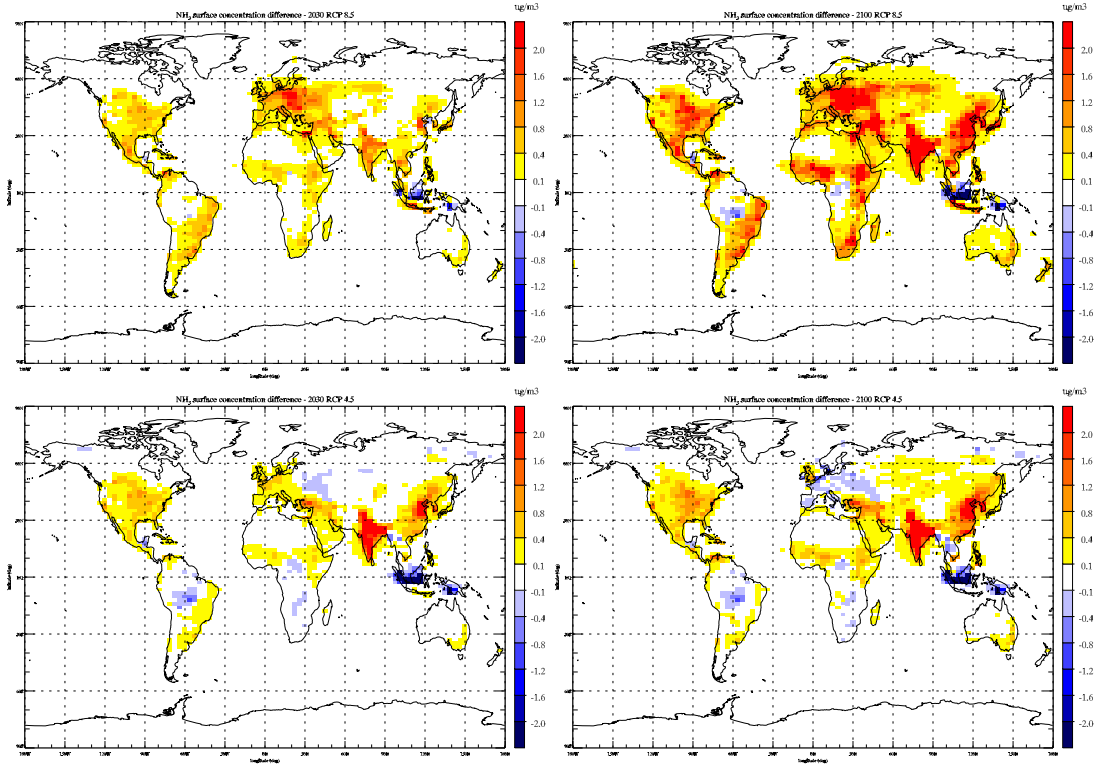

Fig. 15. Changes in ammonia surface concentration ($\mu g\,m^{-3}$) relative to the present-day distribution for scenario RCP8.5 (top) and RCP4.5 (bottom) calculated for 2030 (left) and 2100 (right).

ACPD
14, 6863–6949, 2014

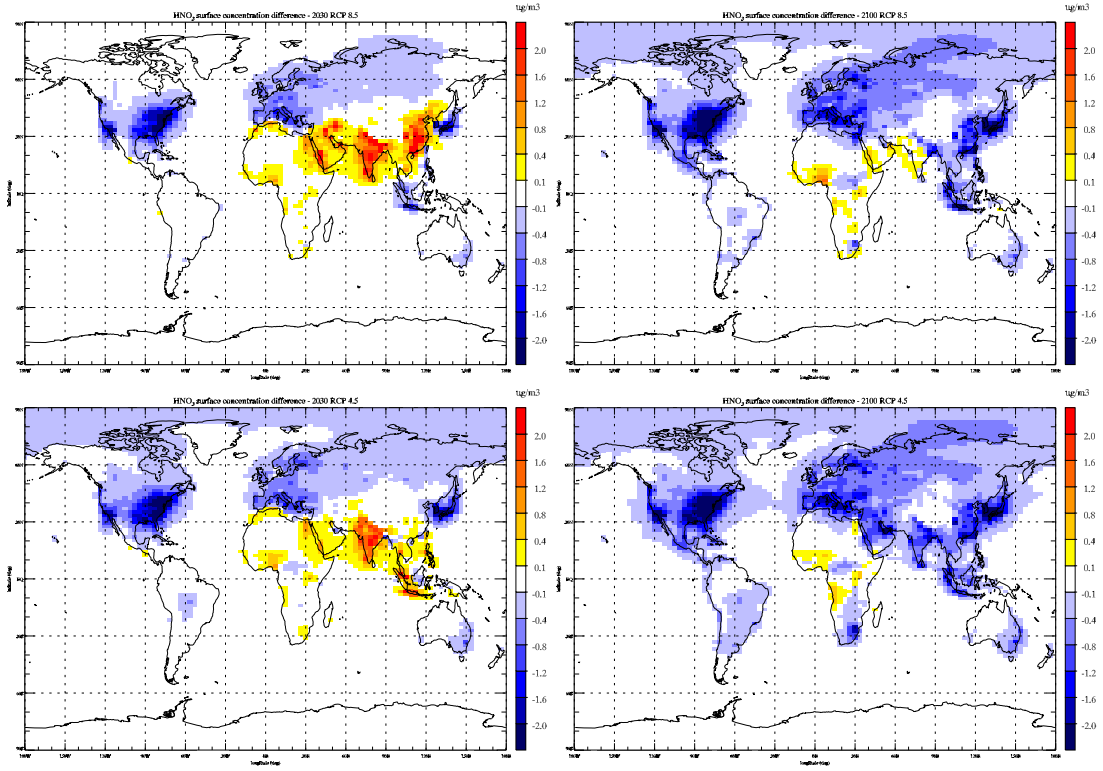

Fig. 16. Changes in nitric acid surface concentration ($\mu g\,m^{-3}$) relative to the present-day distribution for scenario RCP8.5 (top) and RCP4.5 (bottom) calculated for 2030 (left) and 2100 (right).

ACPD
14, 6863–6949, 2014

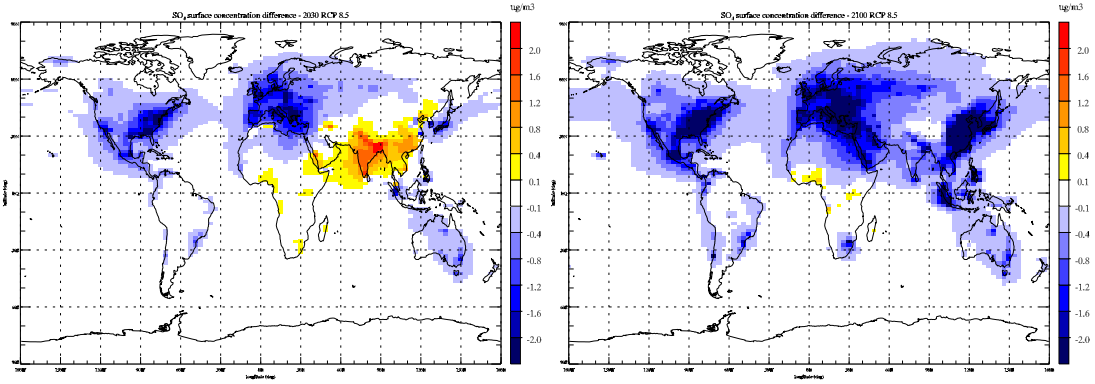

Fig. 17. Changes in sulfates surface concentration ($\mu g\,m^{-3}$) relative to the present-day distribution for scenario RCP8.5 calculated for 2030 (left) and 2100 (right).

ACPD
14, 6863–6949, 2014

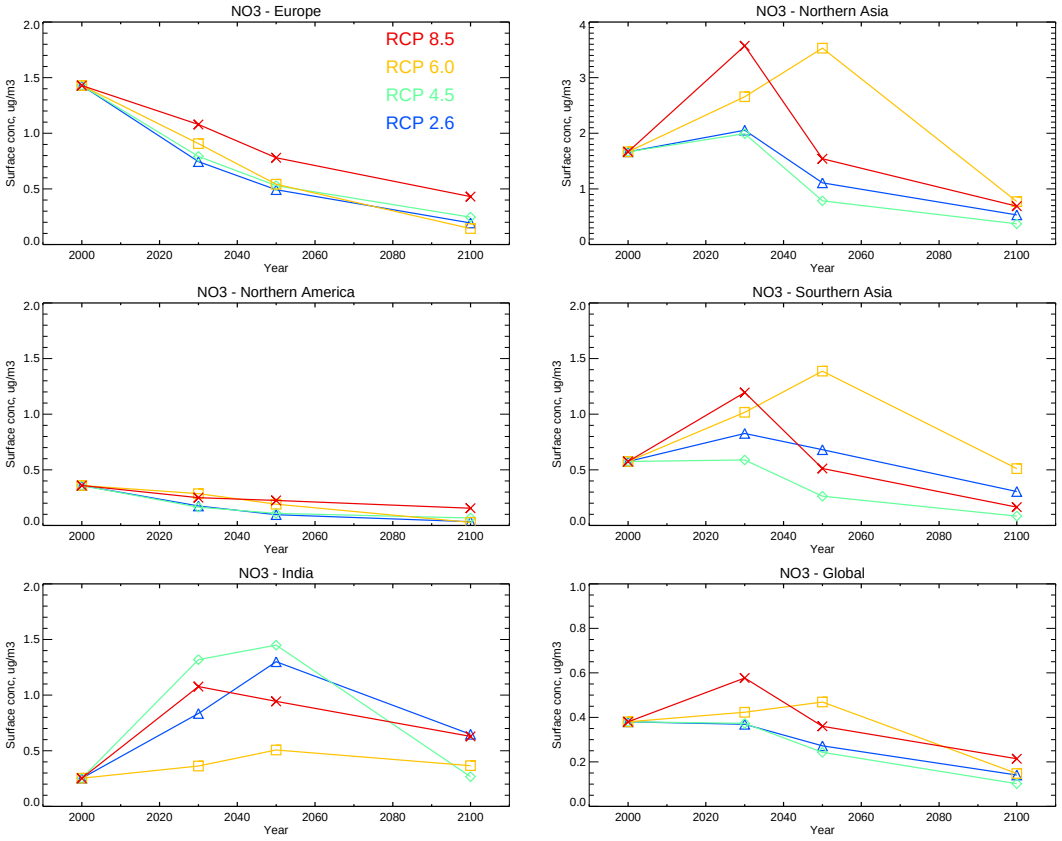

Fig. 18. Evolution of the nitrate surface concentration ($\mu g m^{-3}$) for scenario RCP8.5 (red), RCP6.0 (yellow), RCP4.5 (green) and RCP2.6 (blue) between the present-day and 2100. The averaged surface concentration is depicted for Europe, Northern America, Northern Asia, Southern Asia, India, and the globe.

ACPD
14, 6863–6949, 2014

A global model simulation of present and future nitrate aerosols

D. A. Hauglustaine et al.

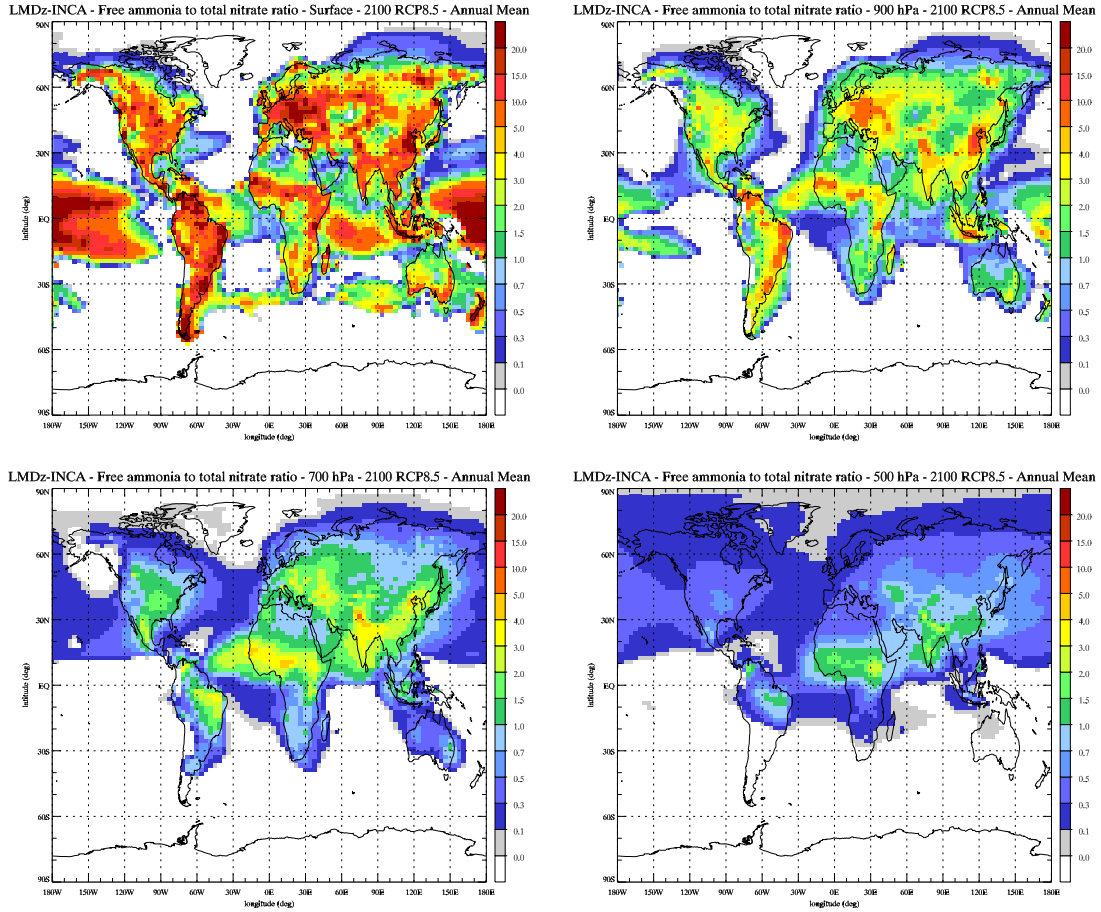

Fig. 19. Annual mean free ammonia to total nitrate ratio calculated for 2100 RCP8.5 conditions at the surface, 900 hPa, 700 hPa, and 500 hPa.

ACPD
14, 6863–6949, 2014

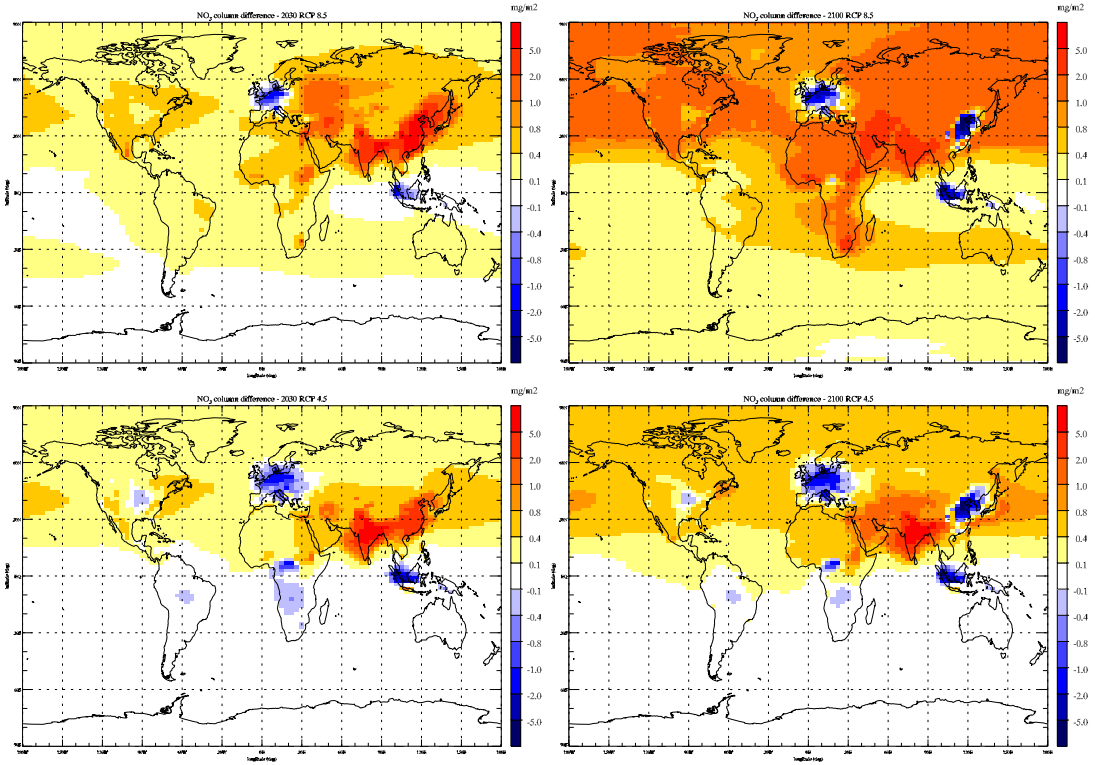

Fig. 20. Changes in nitrate column ($mg\,m^{-2}$) relative to the present-day distribution for scenario RCP8.5 (top) and RCP4.5 (bottom) calculated for 2030 (left) and 2100 (right).

ACPD
14, 6863–6949, 2014

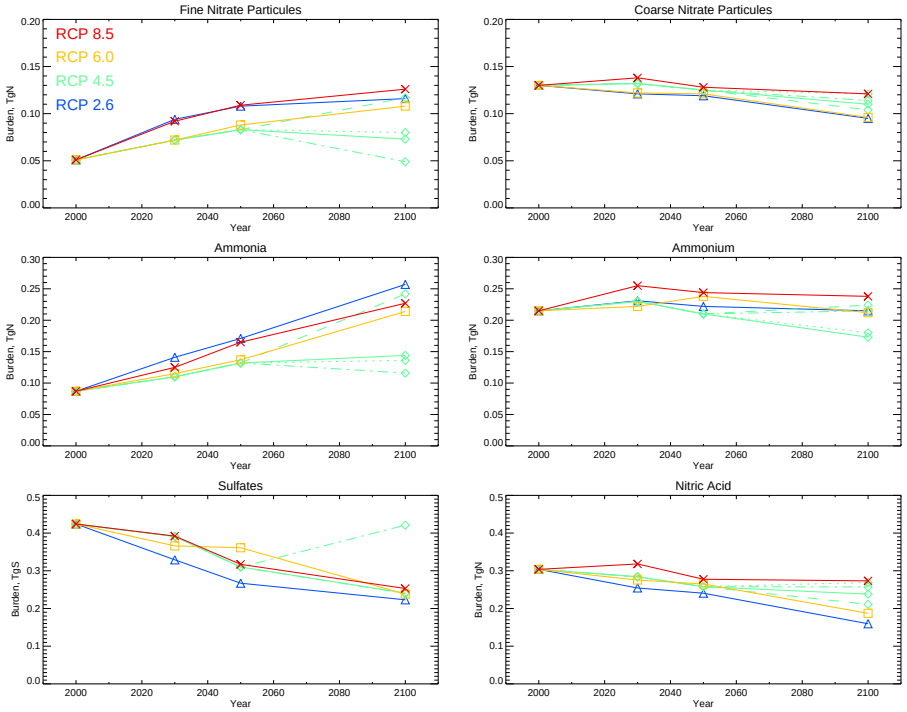

Fig. 21. Evolution of the global burden of fine mode nitrates, coarse mode nitrates, ammonia, ammonium, nitric acid (Tg N), and sulfates (Tg S) for scenario RCP8.5 (red), RCP6.0 (yellow), RCP4.5 (green) and RCP2.6 (blue) between present-day and 2100. The dashed green line refers to the sensitivity scenario RCP4.5-NH_3, the dotted green line to scenario RCP4.5-NO_x, and the dotted-dashed green line to scenario RCP4.5-SO_2.

ACPD
14, 6863–6949, 2014

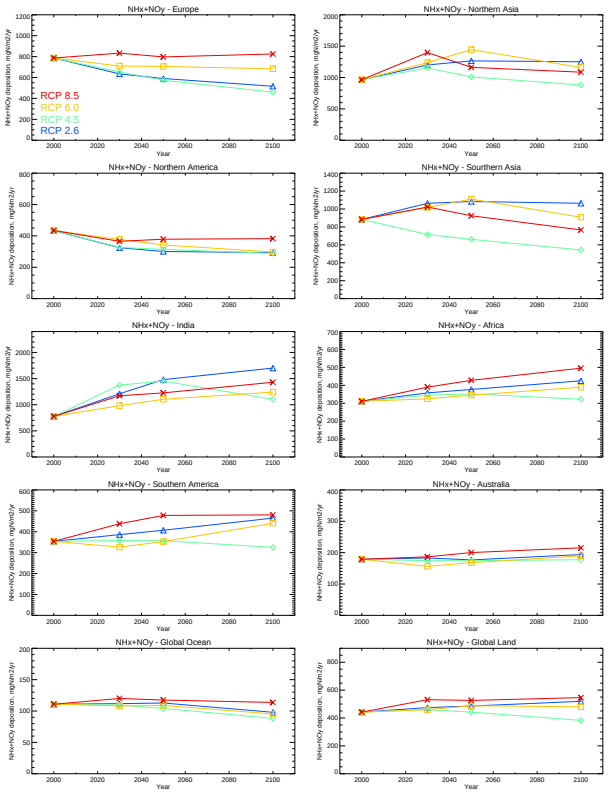

Fig. 22. Evolution of NH_x+NO_y total deposition ($mg\,N\,m^{-2}\,yr^{-1}$) for scenario RCP8.5 (red), RCP6.0 (yellow), RCP4.5 (green) and RCP2.6 (blue) between present-day and 2100. The averaged deposition is depicted for Europe, Northern America, Northern Asia, Southern Asia, India, Africa, Southern America, Australia, the global ocean, and the globe.

ACPD
14, 6863–6949, 2014

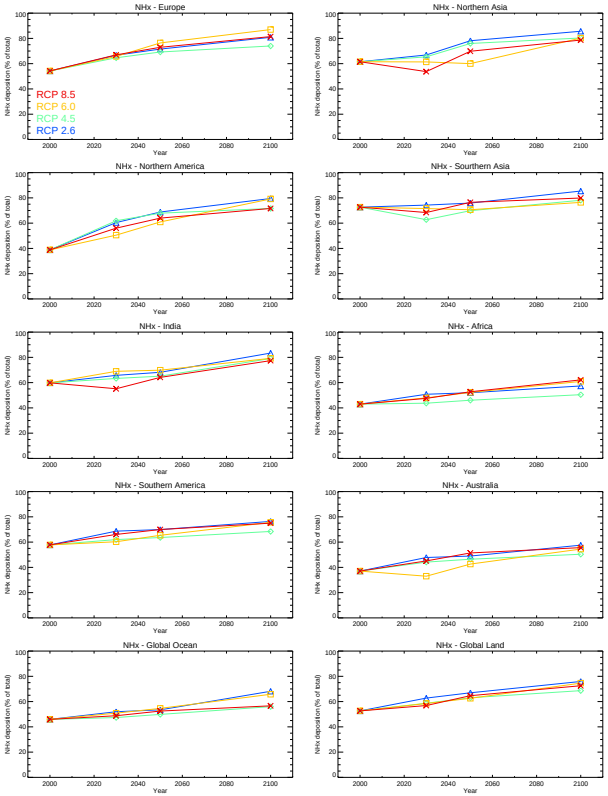

Fig. 23. Evolution of the NH_x fractional contribution to NH_x+NO_y total deposition (%) for scenario RCP8.5 (red), RCP6.0 (yellow), RCP4.5 (green) and RCP2.6 (blue) between present-day and 2100. The averaged deposition is depicted for Europe, Northern America, Northern Asia, Southern Asia, India, Africa, Southern America, Australia, the global ocean, and the globe.

ACPD
14, 6863–6949, 2014

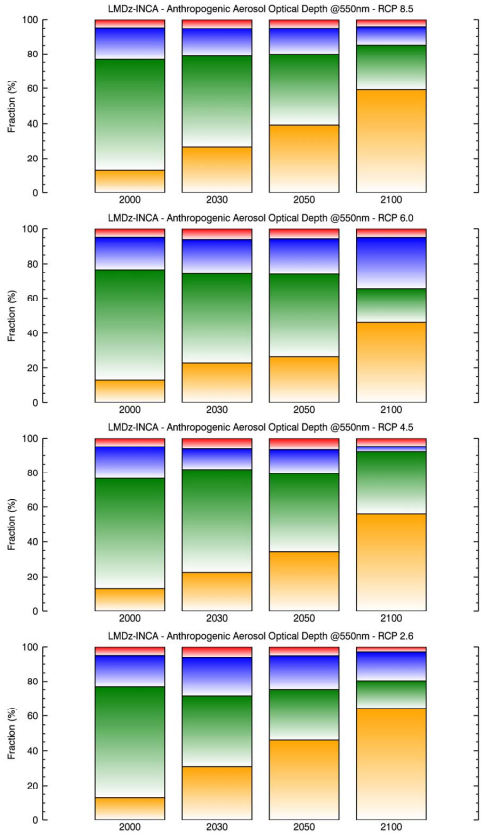

Fig. 24. Evolution of the contribution (%) of nitrates (yellow), sulfates (green), organic carbon (blue), and black carbon (red) to the total aerosol anthropogenic optical depth at 550 nm for the four RCP scenarios and from the present-day to 2100.

ACPD
14, 6863–6949, 2014

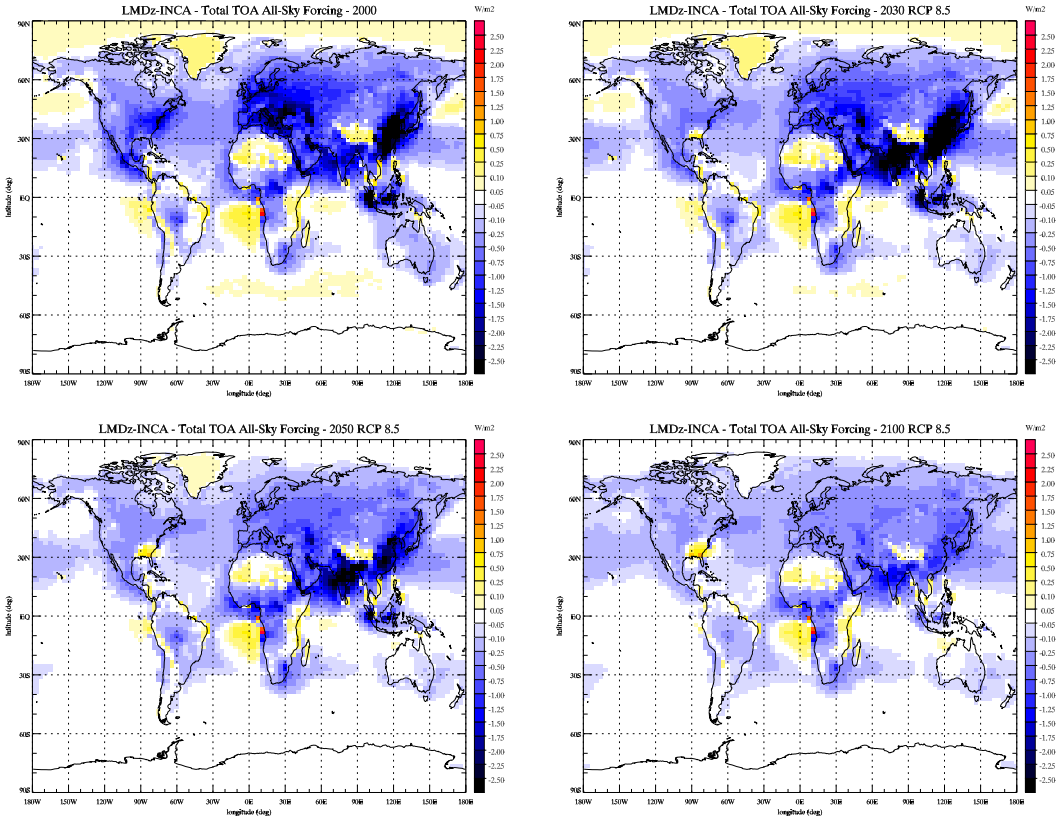

Fig. 25. All-sky top of the atmosphere total direct aerosol radiative forcing ($W m^{-2}$) calculated for the present-day and for 2030, 2050, and 2100 under scenario RCP8.5.

ACPD
14, 6863–6949, 2014

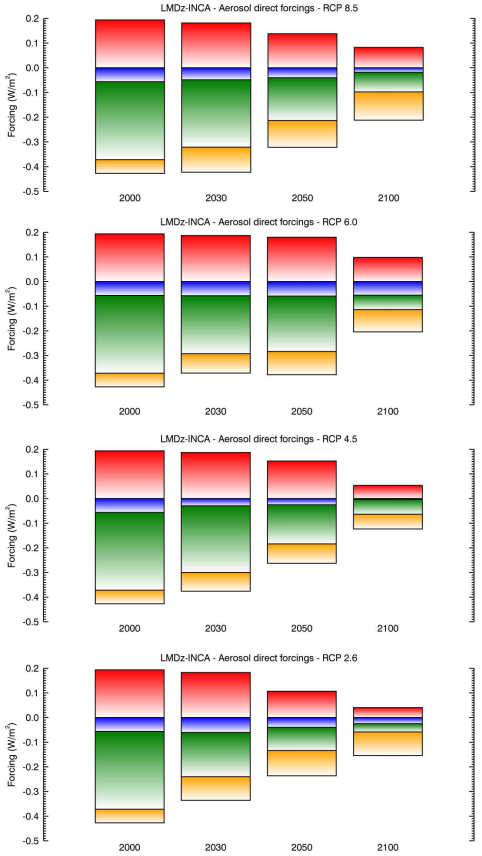

Fig. 26. All-sky top of the atmosphere direct radiative forcing ($W m^{-2}$) of nitrates (yellow), sulfates (green), organic carbon (blue), and black carbon (red) calculated for the four RCP scenarios and from the present-day to 2100.

ACPD
14, 6863–6949, 2014

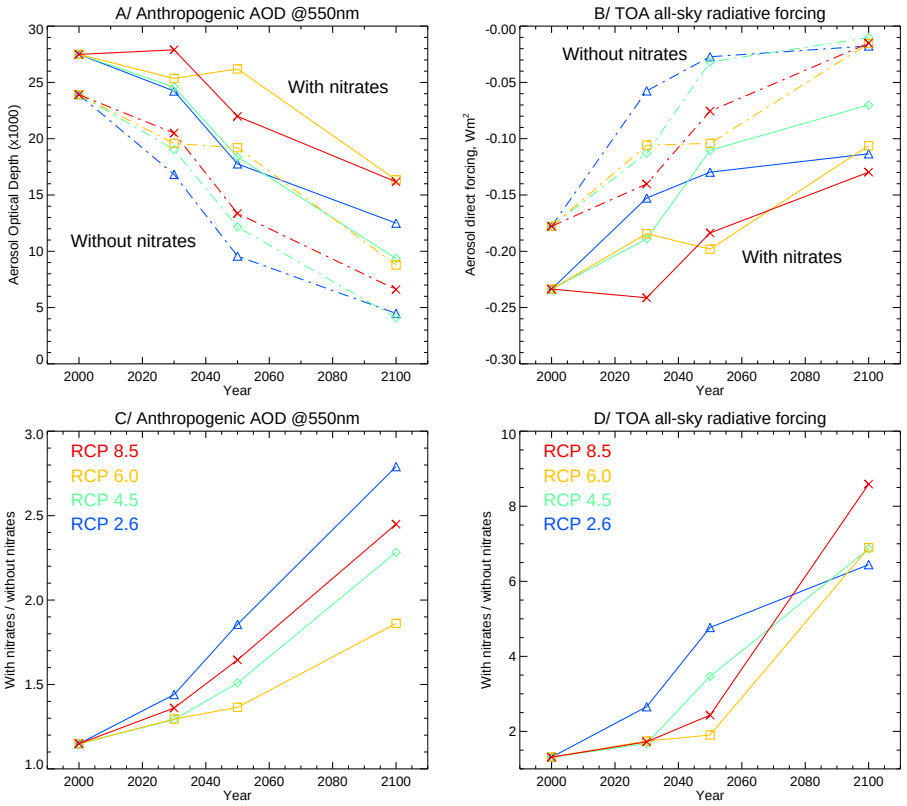

Fig. 27. Evolution of **(A)** the aerosol anthropogenic optical depth at 550 nm (X1000) and **(B)** all-sky top of the atmosphere direct radiative forcing ($W\,m^{-2}$) for the four RCP scenarios and from present-day to 2100; RCP8.5 (red), RCP6.0 (yellow), RCP4.5 (green) and RCP2.6 (blue) Solids lines: nitrates included; dashed lines: nitrates excluded. Corresponding fractional contribution of nitrates to the **(C)** anthropogenic aerosol optical depth and **(D)** direct radiative forcing.

ACPD
14, 6863–6949, 2014